Dynamics and Predictability of the Intensification of Hurricane Edouard (2014)

ERIN B. MUNSELL AND FUQING ZHANG

Department of Meteorology, and Center for Advanced Data Assimilation and Predictability Techniques, The Pennsylvania State University, University Park, Pennsylvania

JASON A. SIPPEL

I. M. Systems Group, Rockville, and National Oceanic and Atmospheric Administration/Environmental Modeling Center, College Park, Maryland

SCOTT A. BRAUN

Laboratory for Mesoscale Atmospheric Processes, NASA Goddard Space Flight Center, Greenbelt, Maryland

YONGHUI WENG

Department of Meteorology, and Center for Advanced Data Assimilation and Predictability Techniques, The Pennsylvania State University, University Park, Pennsylvania

(Manuscript received 11 January 2016, in final form 10 November 2016)

ABSTRACT

The dynamics and predictability of the intensification of Hurricane Edouard (2014) are explored through a 60-member convection-permitting ensemble initialized with an ensemble Kalman filter that assimilates dropsondes collected during NASA's Hurricane and Severe Storm Sentinel (HS3) investigation. The 126-h forecasts are initialized when Edouard was designated as a tropical depression and include Edouard's near–rapid intensification (RI) from a tropical storm to a strong category-2 hurricane. Although the deterministic forecast was very successful and many members correctly forecasted Edouard's intensification, there was significant spread in the timing of intensification among the members of the ensemble.

Utilizing composite groups created according to the near-RI-onset times of the members, it is shown that, for increasing magnitudes of deep-layer shear, RI onset is increasingly delayed; intensification will not occur once a critical shear threshold is exceeded. Although the timing of intensification varies by as much as 48 h, a decrease in shear is observed across the intensifying composite groups ~6–12 h prior to RI. This decrease in shear is accompanied by a reduction in vortex tilt, as the precession and subsequent alignment process begins ~24–48 h prior to RI. Sensitivity experiments reveal that some of the variation in RI timing can be attributed to differences in initial intensity, as the earliest-developing members have the strongest initial vortices regardless of their environment. Significant sensitivity and limited predictability exists for members with weaker initial vortices and/or that are embedded in less conducive environments, under which the randomness of moist convective processes and minute initial differences distant from the surface center can produce divergent forecasts.

1. Introduction

Over the past 5 years, considerable effort has been directed toward improving tropical cyclone (TC) intensity prediction. Despite this effort, the operational prediction of tropical cyclone formation and significant changes in intensity, such as rapid intensification (RI) or decay, remain particularly challenging (Elsberry et al. 2007). These TC forecasts are typically characterized by considerable uncertainty, though past studies have demonstrated the ability of ensemble sensitivity analyses to diagnose the most influential variables contributing to this forecast variance (Torn and Hakim 2009; Torn et al. 2015; Komaromi et al. 2011; Brown and Hakim 2015).

This study utilizes a 60-member convection-permitting ensemble forecast of Hurricane Edouard (2014) initialized at 1200 UTC 11 September 2014 to examine the forecast

Corresponding author e-mail: Professor Fuqing Zhang, fzhang@psu.edu

DOI: 10.1175/JAS-D-16-0018.1

uncertainty and errors associated with the period of near-RI of Edouard. The forecast was a real-time product of the Pennsylvania State University (PSU) hurricane forecast and analysis system, which benefits from its capability to assimilate airborne Doppler radar observations as well as other more traditional reconnaissance observations in near–real time using an ensemble Kalman filter (EnKF). The ensemble forecasts of Edouard in particular are aided by the assimilation of extensive observations taken during the National Aeronautics and Space Administration's (NASA) Hurricane and Severe Storm Sentinel (HS3) mission (Braun et al. 2016). These same observations, when not assimilated, can be used for model verification.

The tropical wave that eventually became Edouard exited the African coast on 6 September (Stewart 2014). A broad area of low pressure and disorganized convection traveled westward for ~4 days until convection began to increase near the surface center late on 10 September. Edouard was subsequently designated as a tropical depression the following day, and slow but steady strengthening led to Edouard becoming a tropical storm early on 12 September. Upper-level winds and sea surface temperatures remained favorable for further intensification, although dry air in the surrounding environment may have slowed the intensification rate as Edouard tracked northwestward. As Edouard reached hurricane status on 14 September, a period of near-RI occurred, in which the maximum 10-m sustained winds increased by 12.9 m s^{-1} (25 knots) over the succeeding 24 h period.[1] Just prior to the end of the simulation window, Edouard reached peak intensity as a major hurricane, the first in the Atlantic basin since Hurricane Sandy in 2012. Just beyond the simulation window, Edouard maintained major hurricane status only briefly before sharply weakening during an eyewall replacement cycle as the storm began to move northward. As the TC accelerated toward the northeast and became embedded in the midlatitude westerlies, a period of rapid weakening commenced, and by 19 September Edouard had degenerated into a remnant low.

Although the official forecast intensity errors were lower than the mean official errors for the previous 5-yr period at all forecast times, there was a persistent bias leading up to Edouard's near-RI period in which the official forecast underestimated[2] the intensity of the TC (Stewart 2014). Such errors are typical since anticipating significant changes in intensity, such as RI, is challenging because it depends on both the chaotic dynamics of the TC inner core and the more easily observed large-scale environmental and ocean conditions. Statistical predictions of RI attempt to account for all of these influences (e.g., Kaplan and DeMaria 2003; Kaplan et al. 2010) though such methods may be limited because of a strong dependence on the large-scale environment, rather than more detailed inner-core information.

The environment can also limit the predictability of RI when large-scale variables are in a sensitive regime in which development or nondevelopment are possible with similar likelihoods. In particular, moderate vertical wind shear has been found to strongly modulate tropical cyclone predictability (Zhang and Tao 2013; Tao and Zhang 2014), probably because of resultant uncertainty in the evolution of vortex tilt. Vertical wind shear is known to cause TC vortices to become tilted downshear left (Reasor and Montgomery 2001; Corbosiero and Molinari 2002; Rogers et al. 2003; Braun et al. 2006; Braun and Wu 2007), which subsequently helps create an asymmetry in which convection is enhanced downshear and suppressed upshear (e.g., Frank and Ritchie 1999; Black et al. 2002; Corbosiero and Molinari 2002, 2003; Chen et al. 2006; Braun et al. 2006; Braun and Wu 2007). The tilt vector of a sheared TC can undergo a precession process, in which the tilt rotates cyclonically until the angle between the shear and tilt vectors exceeds 90°. If the tilt vector proceeds into the upshear quadrant, near-immediate alignment of the vortex follows (e.g., Reasor et al. 2004; Rappin and Nolan 2012). Changes in tilt relative to the shear will undoubtedly cause changes in the distribution of convection, and Rogers et al. (2016) showed that RI is associated with an increase in convection in the upshear-left quadrant. Though RI typically begins as the vortex aligns, an aligned vortex can also sometimes be a result of RI rather than a trigger (Chen and Gopalakrishnan 2015). Regardless, the speed at which a developing TC vortex completes precession can be accelerated or slowed by random moist convection near the inner-core region (Frank and Ritchie 2001; Zhang and Tao 2013; Tao and Zhang 2014), which limits the predictability under moderate shear.

The PSU deterministic forecast and the majority of the members analyzed in this study were more successful at capturing the correct rate and peak intensity of Edouard, although considerable uncertainty existed in the exact timing of RI onset. Therefore, the primary goal of this study is to utilize the 60-member PSU real-time forecast of Edouard to examine both the environmental factors and the variance in the structural evolution of

[1] Although Edouard did not officially undergo RI (according to the NHC criteria), the period of intensification was significant (a near-RI event). Therefore, we look at RI timing in this ensemble as it is traditionally defined, because it is more straightforward to do so.

[2] It should be noted that NHC is often conservative about forecasting RI unless there are strong indicators it will occur.

the ensemble vortices that resulted in the RI-onset uncertainty.

Section 2 describes the PSU real-time hurricane forecast and analysis setup, operational data examined, and the sensitivity experiment methodology. Section 3 presents the composite analyses of Edouard's intensity forecasts according to RI-onset time as well as results from a series of sensitivity experiments. Finally, section 4 highlights the main conclusions from this study.

2. Methodology and data

a. PSU Atlantic hurricane forecast and analysis system

The deterministic and 60-member ensemble simulation of Hurricane Edouard analyzed in this study was originally a real-time forecast generated by the PSU real-time Atlantic hurricane forecast and analysis system (Zhang et al. 2009, 2011; Zhang and Weng 2015; Weng and Zhang 2016). The 2014 version of this system employed version 3.5.1 of the Advanced Research version of the WRF Model (ARW; Skamarock et al. 2008) and an EnKF data assimilation algorithm. Data assimilated into this system include Global Telecommunication System (GTS) conventional data and reconnaissance data, including superobservations generated from the airborne tail Doppler radar (TDR) on NOAA's P-3 aircraft (Weng and Zhang 2012) and satellite-derived winds (Weng and Zhang 2016). In addition, dropsondes deployed from the NOAA–National Center for Atmospheric Research (NCAR) Advanced Vertical Atmospheric Profiling System (AVAPS) during HS3 flights (Braun et al. 2016) are also assimilated. Three two-way nested Mercator-projected domains are utilized with horizontal grid spacing of 27, 9, and 3 km, which contain 378 × 243, 297 × 297, and 297 × 297 grid points, respectively. The outer domain is fixed and includes the majority of North America and the North Atlantic Ocean, while the inner domains move with the surface vortex of the TC of interest. All three domains contain 43 vertical levels with the top level at 10 hPa. The WRF Model physics configurations are identical to those in Munsell et al. (2015) and Zhang and Weng (2015).

Using operational Global Forecast System (GFS) analysis, the PSU WRF–EnKF system was first initialized at 0000 UTC 4 September; Edouard had recently been designated as an NHC invest area at this time. After 12 h of ensemble integration, the first data assimilation was performed on all three domains at 1200 UTC 4 September, and continuous cycling was performed every 3 h until the dissipation of Edouard. As in all forecasts produced by the PSU WRF–EnKF system, ensemble initial and lateral boundary conditions were generated by adding perturbations derived from the background error covariance of the WRF variational data assimilation system (Barker et al. 2004) to the pressure, temperature, moisture, and horizontal wind fields of the initial and boundary conditions. The EnKF analysis perturbations from 1200 UTC 11 September were used to initialize the ensemble forecasts analyzed in this study.

b. HS3 observations of Hurricane Edouard

Four flights utilizing an unmanned Global Hawk aircraft were conducted throughout all stages of the lifetime of Hurricane Edouard during the 2014 HS3 campaign. Braun et al. (2016) describe the structure and evolution of Edouard during the period of the first two flights that are of most relevance here. These two flights were performed during the 5-day simulation window analyzed in this study. A total of 61 usable AVAPS dropsondes (Wick 2015) were deployed on the 11–12 September flight, and 80 were deployed on the 14–15 September flight (Young et al. 2016). These dropsondes were not assimilated for the real-time ensemble forecast in this study (since they had not been collected yet) and thus are used to independently verify the accuracy of the Edouard simulations.

c. Composite sensitivity experiments: Initial-condition construction

To examine the relative importance of larger-scale environmental conditions versus vortex-scale structure on RI onset, a series of sensitivity experiments is performed whose initial conditions are generated according to the following methodology (results are presented in sections 3e and 3f). First, groups of members are created according to their RI-onset time (GOOD_EARLY, GOOD, GOOD_LATE, and POOR). Next, composited initial conditions created by averaging the initial conditions in each group are used to initialize additional simulations. For each composite, more sets of initial conditions are generated by replacing all fields at all vertical levels within a given radius from the surface center of Edouard with the fields from different sets of composited initial conditions. Linear blending is performed about the radius at which the initial conditions are combined in order to prevent sharp discontinuities, and the resulting initial conditions are then used to run simulations in an otherwise identical experiment to that of the original ensemble. Descriptions of the sensitivity experiment initial conditions and the blending radii are summarized in Table 1.

A final experiment is designed to test the sensitivity of RI onset to the moisture field within the region of greatest sensitivity in the POOR environment. This experiment, EnvGoodTcPoor800DiffQ (Table 1), is

TABLE 1. Summary of the sensitivity experiments that are discussed in sections 3e and 3f.

Experiment name	Inner region	Outer region	Blending radii (km)	Does RI occur?
EnvGoodEarlyTcGood	GOOD	GOOD_EARLY	200–300	Yes, 72 h
EnvGoodEarlyTcPoor	POOR	GOOD_EARLY	200–300	Yes, 72 h
EnvGoodTcGoodEarly	GOOD_EARLY	GOOD	200–300	Yes, 48 h
EnvPoorTcGoodEarly	GOOD_EARLY	POOR	200–300	Yes, 72 h
EnvGoodTcPoor	POOR	GOOD	200–300	Yes, 72 h
EnvGoodTcPoor500	POOR	GOOD	400–600	Yes, 72 h
EnvGoodTcPoor600	POOR	GOOD	500–700	Yes, 72 h
EnvGoodTcPoor650	POOR	GOOD	500–800	Yes, 72 h
EnvGoodTcPoor700	POOR	GOOD	600–800	No
EnvGoodTcPoor800	POOR	GOOD	700–900	Yes, 72 h
EnvGoodTcPoor900	POOR	GOOD	800–1000	No
EnvGoodTcPoor1100	POOR	GOOD	1000–1200	No
EnvPoorTcGood	GOOD	POOR	200–300	No
EnvPoorTcGood500	GOOD	POOR	400–600	No
EnvPoorTcGood600	GOOD	POOR	500–700	No
EnvPoorTcGood650	GOOD	POOR	500–800	No
EnvPoorTcGood700	GOOD	POOR	600–800	No
EnvPoorTcGood800	GOOD	POOR	700–900	No
EnvPoorTcGood900	GOOD	POOR	800–1000	Yes, 72 h
EnvPoorTcGood1100	GOOD	POOR	1000–1200	Yes, 72 h
EnvGoodTcPoor800DiffQ	POOR	GOOD	700–900	No

identical to EnvGoodTcPoor800 except for the moisture fields within the blending radii (700–900 km). The differences between the moisture fields in this sensitivity experiment depend on the radius from the surface center of Edouard and are dictated by this set of equations:

$$\begin{cases} 0, & r < 700\,\text{km} \\ \alpha\Delta Q, & 700 \le r \le 900\,\text{km}, \\ 0, & r > 900\,\text{km} \end{cases}$$

where r is the radius from the storm center (km), α is a scaling factor based on the radius, and ΔQ is the difference between the water mixing ratio fields from the GOOD and POOR composites (GOOD − POOR). The equation for the scaling factor is

$$\alpha = 1 - \left(\frac{900 - r}{100}\right).$$

3. Results and discussion

a. *Overview of the PSU real-time WRF–EnKF ensemble performance*

Since the primary goal of this study is to examine the predictability of the dynamics associated with the near-RI of Hurricane Edouard, the 126-h forecast chosen for analysis was initialized at the time of the storm's designation as a tropical depression and was integrated through intensification (1200 UTC 11 September–1800 UTC 16 September). Figure 1a shows the corresponding plot of Edouard's best track, as defined by the NHC, as well as the tracks of the control run (APSU) and ensemble members from the PSU WRF–EnKF forecasting system. The associated minimum SLP (hPa, Fig. 1b) and the 10-m maximum wind speed (kt, Fig. 1c) evolution are also presented. Considering the lead time prior to intensification, the APSU deterministic forecast is quite successful; the track closely follows that of the best track, and both the onset time and the rate of intensification (in terms of SLP and maximum 10-m winds) during the near-RI event are comparable. A slight negative bias in the minimum SLP forecast is consistent with a known bias in the forecasting system that results from uncertainty in the representation of surface fluxes (Green and Zhang 2013). In addition, the majority of ensemble members ultimately reach the correct intensity, although there is significant spread (as much as 48–60 h) in the timing of RI onset. Furthermore, some ensemble members fail to intensify during the 126-h forecast, which facilitates examining the causes for large uncertainty. The causes for the significant spread in the timing of RI will be investigated in order to assess the predictability associated with the governing dynamics of the near-RI event of Edouard.

As in previous ensemble sensitivity studies (Munsell et al. 2013, 2015; Munsell and Zhang 2014), the variations among the members that lead to the considerable divergence in RI-onset time are identified through creating 10-member composite groups based on the timing of intensification. In this study, the RI-onset time of each member is defined as the time at which the subsequent

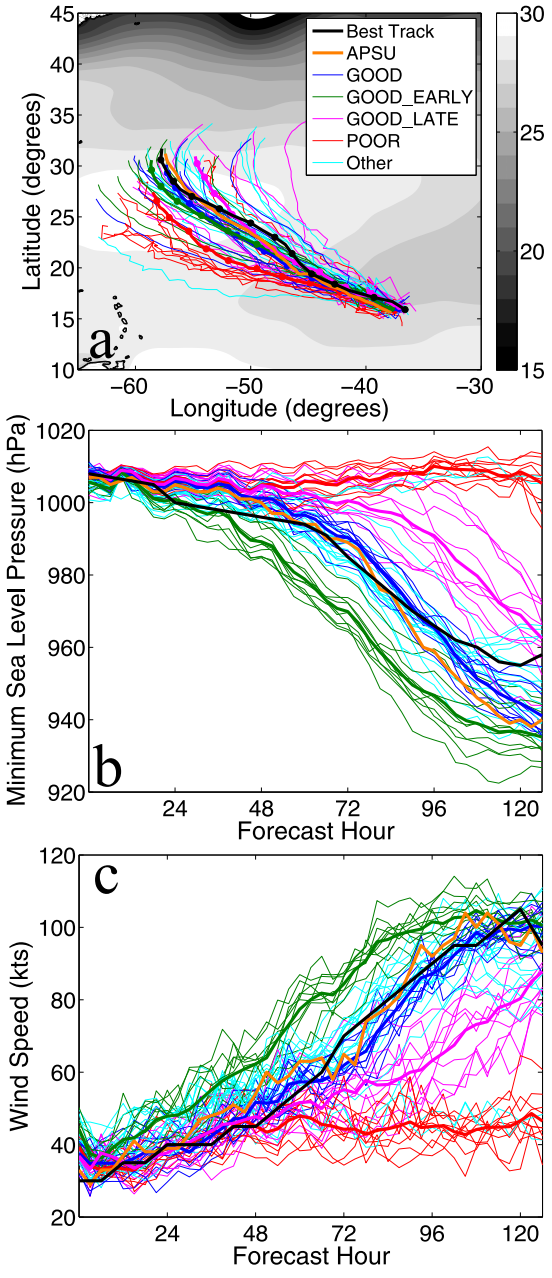

FIG. 1. A comparison of the best track with 5-day deterministic and ensemble forecasts of (a) track, (b) minimum SLP (hPa), and (c) maximum 10-m wind speed (knots; 1 kt = 0.51 m s^{-1}) forecasts for the 1200 UTC 11 Sep 2014 initialization of Hurricane Edouard from the PSU WRF–EnKF system. Members are placed in composite groups of 10 according to their RI-onset time. Members in GOOD begin RI onset close to the observed time (72 h; blue), those in GOOD_EARLY begin RI 24 h earlier (48 h; green), those in GOOD_LATE begin 24 h after the observed time (96 h; magenta), and in POOR RI does not occur in the simulation window (red). The composite means [thick; positions marked every 12 h in (a)], the NHC best track [black; positions marked every 12 h in (a)], and the APSU deterministic forecast (orange) are also plotted. The remaining ensemble members not classified in composite groups are in cyan. Sea surface temperatures (constant throughout simulation) are contoured (gray shading every 1°C, starting at 15°C) in (a).

24-h intensity change is maximized. The 10 members whose RI-onset times are closest to that of the best track RI onset (~1200 UTC 14 September, or 72 h simulation time) comprise the group GOOD, while two additional clusters of 10 members that begin RI 24 h prior to and 24–36 h after the best track RI are classified as the composite groups GOOD_EARLY and GOOD_LATE, respectively. The final composite group POOR consists of 10 members that fail to intensify throughout the simulation. Because a limited number of simulations fail to intensify, each group is restricted to 10 members to allow for equal-member groups for compositing. Therefore, 40 of the 60 ensemble members are placed in one of the composite groups.

Figure 1 shows the ensemble-member forecasts colored by composite group, along with the mean track and intensity of each composite. The evolution of the mean intensity in each group clearly illustrates that the three developing composite groups have similar rates of intensification and primarily differ only in the timing of their RI onset (Figs. 1b,c). Note that the mean tracks of these developing groups are more closely aligned with the best track, while the mean track of POOR has a more westward component of motion (Fig. 1a), likely as a result of a shallower layer of easterly winds that steer the motion of the weaker POOR vortices (Velden and Leslie 1991). Before continuing with the analysis to determine the causes of the significant ensemble RI-onset-time uncertainty, the GOOD composite group is first evaluated against HS3 observations to assess the representativeness of the WRF–EnKF simulation.

b. *Comparison of HS3 observations and WRF–EnKF ensemble*

For this particular ensemble, in which the predictability of Edouard's RI is highly uncertain, validation of the ensemble is very important. For this reason, we compare available HS3 dropsonde data from 11–12 September with the mean of the GOOD composite members in Fig. 2. Observed and simulated vertical profiles of relative humidity (Figs. 2a,d), zonal (Figs. 2b,e), and meridional components of wind (Figs. 2c,f) at 18 and 24 h are shown along with root-mean-square difference (RMSD) profiles between the dropsondes and the simulations. Observations collected within 90 min of the given time were averaged to produce the observational profiles, while the simulated profiles were generated by extracting and averaging the vertical profiles at each of the model grid points that were closest to the storm-relative locations at which the observations were obtained. In addition, Fig. 3 compares the spatial distribution of the simulated and observed environments by overlaying storm-centered GOOD composite means

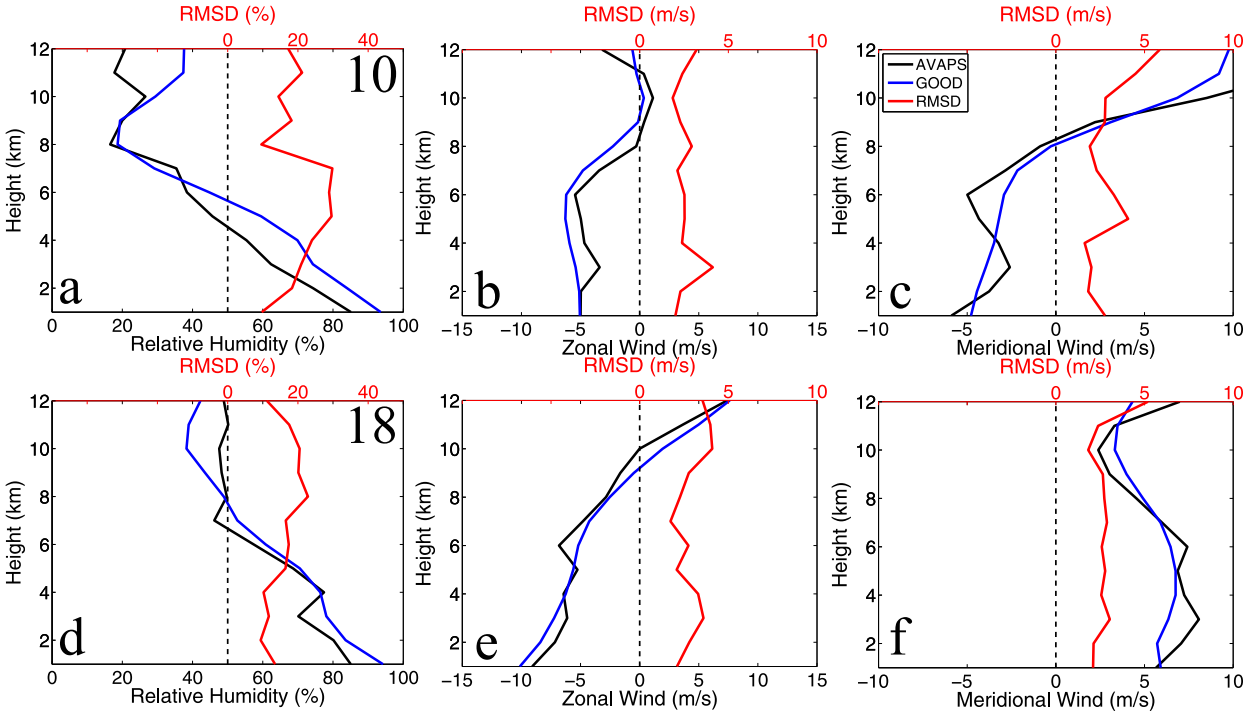

FIG. 2. Composite vertical profiles of (a),(d) relative humidity (%), (b),(e) zonal winds ($m\,s^{-1}$), and (c),(f) meridional winds ($m\,s^{-1}$) for the AVAPS dropsondes (black), GOOD (blue), and the RMSD between them (red) at (top) 0600 UTC 12 Sep (18 h) and (bottom) 1200 UTC 12 Sep 2014 (24 h). Numbers in the top-right corners of (a) and (d) correspond to the number of profiles used to make the composites at that time.

of the 700-hPa relative humidity and 950-hPa wind speed with observations from the AVAPS dropsondes.

The moisture field in GOOD is generally in good agreement with HS3 dropsondes, though there are larger discrepancies in the vicinity of moisture gradients. About half of the dropsondes used to verify 18-h forecast in Figs. 2a–c are near or within the very sharp moisture gradients in the forecast, which explains the large relative humidity RMSD at that time, as compared with 24 h (cf. Figs. 2a and 2d). Despite these differences, the forecast and dropsondes show a similar spatial distribution of moisture, with midlevel dry air wrapping around the north, west, and south sides of the TC and very moist air near the surface circulation center. Though there appears to be a slight 700-hPa moist bias in some areas of Fig. 3a, a comparison between the dropsondes and the simulation of this environmental dry air at 500 hPa yields more agreement (not shown).

The WRF–EnKF simulation also appears to be representative of the observed TC vortex in the early stages of its intensification. Differences in both wind components in Fig. 2 are generally smaller than 2–4 $m\,s^{-1}$, and there is no obvious bias. In addition, RMSDs between the profiles are less than 5 $m\,s^{-1}$ at all vertical levels and both times. The overall structure of the vortex in Fig. 3b is also well represented in the model, with the maximum winds located just to the northeast of the surface circulation and embedded within a fairly broad region of tropical storm–strength winds. There is good agreement on the very asymmetric circulation of Edouard, with considerably weaker winds to the south of the surface center at this time. The simulated winds are also somewhat weaker than what was observed in the region of maximum winds by ~5 $m\,s^{-1}$.

c. *Exploring the significant ensemble RI-onset variability: Impacts of initial vortex strength*

Although the WRF–EnKF ensemble of Hurricane Edouard is created through the application of small perturbations to the initial conditions, the simulation produces developing TCs with a significant range of RI-onset times. This ensemble variance is first explored by analyzing differences in initial vortex strength. Past studies have shown that initially stronger or larger vortices tend to intensify more quickly because they are able to resist negative environmental influences (Jones 1995; Reasor et al. 2004; Sippel et al. 2011; Torn and Cook 2013), which can potentially impact the timing of RI onset. To examine the evolution of the strength of the TC vortices, the low-level (850–700 hPa) layer-averaged

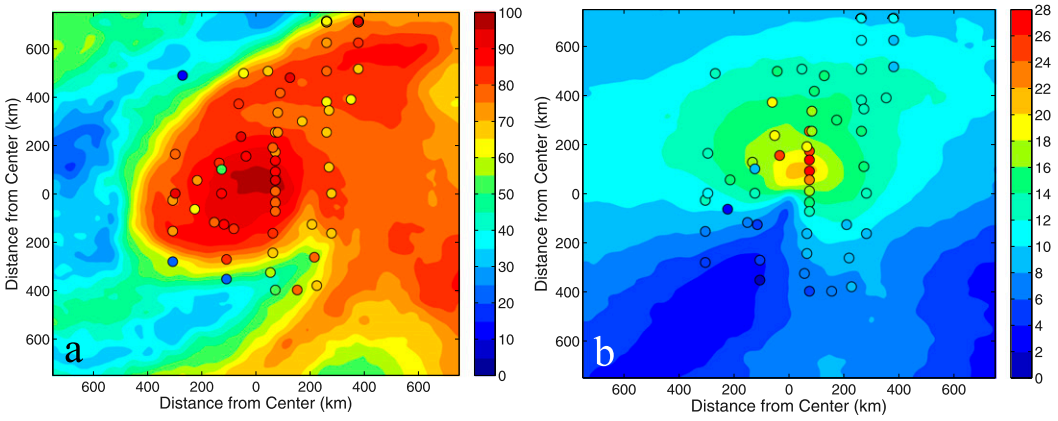

FIG. 3. (a) Storm-centered horizontal cross section of 700-hPa relative humidity (contours filled every 5%) for the GOOD composite group at 0900 UTC 12 Sep 2014 (21 h). Markers indicate storm-centered positions of the AVAPS dropsondes that were deployed during the 12 Sep HS3 flight and are filled according to the value of relative humidity recorded closest to 700 hPa. (b) As in (a), but for 950-hPa winds (contours filled every 2 m s^{-1}).

(within a 250-km radius of the 775-hPa center) relative vorticity is calculated for each of the composite groups (Fig. 4a). The ensemble evolution suggests that the initial vortex intensity may have contributed to the RI timing of Edouard, as the GOOD_EARLY composite members consistently have low-level vorticity magnitudes stronger than that of the other composite members throughout much of the first 48 h of the simulation. Over the remaining 3 days of the simulation, the developing members approach and undergo RI, and the relative vorticity in GOOD_EARLY, GOOD, and GOOD_LATE gradually increases accordingly, while the composite-mean POOR relative vorticity actually decreases.

The relationship of the RI-onset time with both minimum SLP and low-level, area-average vorticity further supports the impact of the initial vortex strength on the subsequent evolution (Fig. 4b). The magnitude of initial correlation for both metrics is about 0.25, which falls just under the level of statistical significance, suggesting a very weak tendency for the stronger vortices to begin RI sooner. However, the correlation steadily increases as the vortices evolve, becoming statistically significant by 3–6 h and approaching more moderate to strong values through 36 h. This suggests that part of the variance in RI onset can be explained by differences in vortex strength that exist from very early on in the simulation.

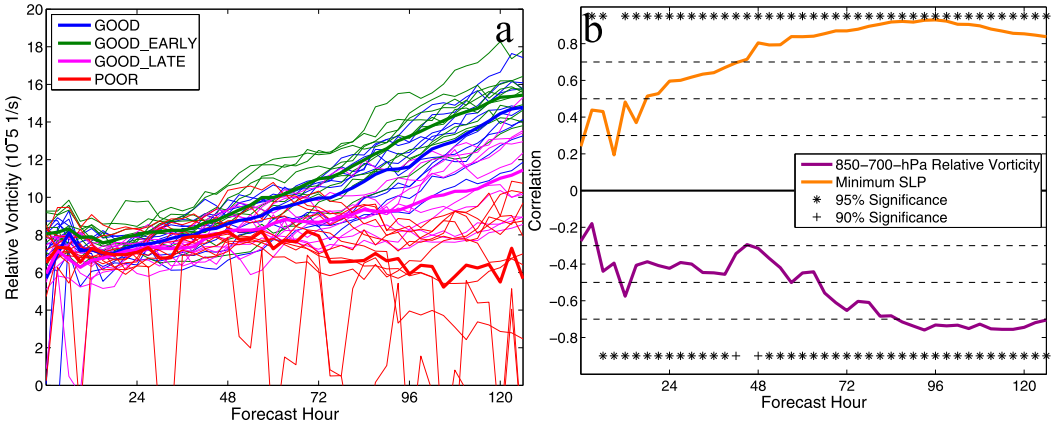

FIG. 4. (a) Evolution of the layer-averaged low-level (850–700 hPa; within a 250-km radius of the 775-hPa center) relative vorticity (10^{-5} s^{-1}) for the mean (thick) and individual ensemble members (thin) of the composite groups GOOD (blue), GOOD_EARLY (green), GOOD_LATE (magenta), and POOR (red). (b) Evolution of the correlation between both the layer-averaged low-level relative vorticity and the minimum SLP and the RI-onset time utilizing the 30 members of the developing composite groups. Correlation that is significant at the 95% (90%) significance level is indicated by asterisks (plus signs).

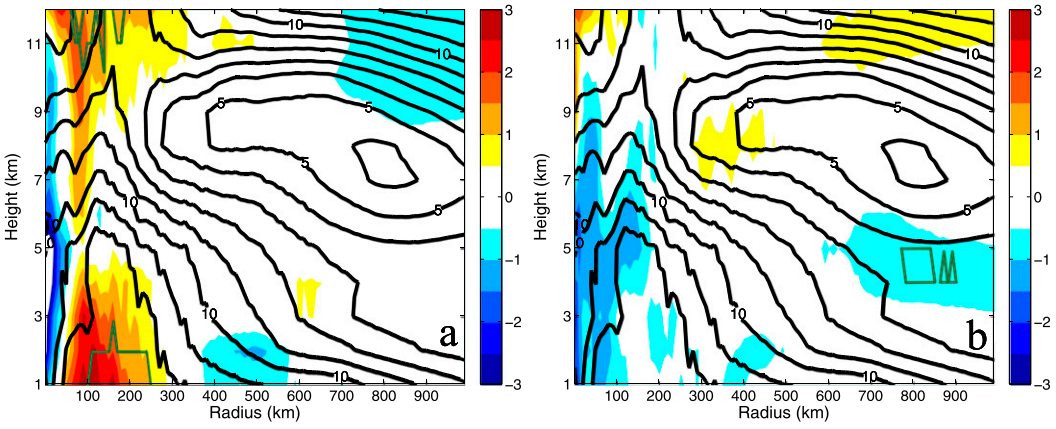

FIG. 5. (a) Azimuthally averaged vertical cross section of tangential winds at 0 h for the GOOD composite (contoured every 1 m s^{-1}; black) overlaid with differences (filled contours every 0.5 m s^{-1} between −3 and 3 m s^{-1}) between the GOOD_EARLY and the GOOD initial vortex (GOOD_EARLY–GOOD). Regions of statistical significance at the 95% confidence level are also contoured in green. (b) As in (a), but differences are between the initial vortex of GOOD and POOR.

The wind structure of GOOD_EARLY vortices also reveals that they are initially stronger through much of the troposphere. The vertical structure of the vortices is examined through azimuthally averaged vertical cross sections of tangential winds and the associated differences between the composites (Fig. 5). The tangential winds of the GOOD composite vortex peak at ~12 m s^{-1} near the surface at a radius between 100 and 200 km. In addition, as is standard in warm-core vortices, the tangential winds decay with both radius and height. The differences in tangential wind structure between GOOD_EARLY and GOOD reveal that the initial GOOD_EARLY circulation is as much as 3 m s^{-1} stronger than GOOD, and the difference in strength is statistically significant both near the surface and in the upper troposphere (Fig. 5a). Since GOOD_EARLY vortices are initially stronger, it is speculated that they are likely more resilient to environmental influences and thus able to align and undergo RI the earliest.

Meanwhile, initial vortex strength apparently cannot explain the differences among the remainder of the composites. A vertical cross section of tangential wind differences between GOOD and POOR (Fig. 5b) demonstrates that the initial strength of those two vortices is quite similar; the small differences within the radius of maximum winds are not statistically significant. Comparisons between vertical cross sections of relative humidity and temperature between GOOD and POOR also reveal very few significant differences in these fields (not shown). The starkly different outcomes in GOOD and POOR despite initially similar vortex strengths and thermodynamic environments in the inner-core region suggest that the POOR members have larger-scale environments that are less conducive for intensification.

d. *Significant ensemble RI-onset variability: Impacts of deep-layer shear on vortex evolution*

Although the differences in initial vortex strength can explain some of the variability present in the RI-onset times of the Edouard ensemble, deep-layer vertical wind shear has a stronger influence on the timing of RI among the composites. Given the strong dependence of the predictability of an RI event on the magnitude of deep-layer vertical wind shear (Tao and Zhang 2014, 2015), the evolution of the area-averaged (between 200 and 800 km from the surface center) deep-layer (850–200 hPa) wind shear magnitude (Fig. 6a) and direction (Fig. 6f) among the composite groups is examined. Observational shear values obtained from the Statistical Hurricane Intensity Prediction Scheme (SHIPS; DeMaria et al. 2005) are also included, which are in mostly good agreement with the GOOD shear evolution. Shear magnitude is relatively weak initially (~6 m s^{-1}) in all composite members, but it steadily increases over the first 24 h to a relatively strong value of 9 m s^{-1}. By 48–60 h, there is a clear separation in the shear magnitudes of the composite groups such that groups with later RI-onset time have stronger shear. There also appears to be a critical shear magnitude threshold (~12 m s^{-1}) in this ensemble, above which most of the ensemble members (primarily POOR) do not undergo RI within the simulation window. Although this ensemble is a real-data case with differences throughout the environment, this shear magnitude limit is comparable to the 12.5 m s^{-1} development threshold derived from the idealized

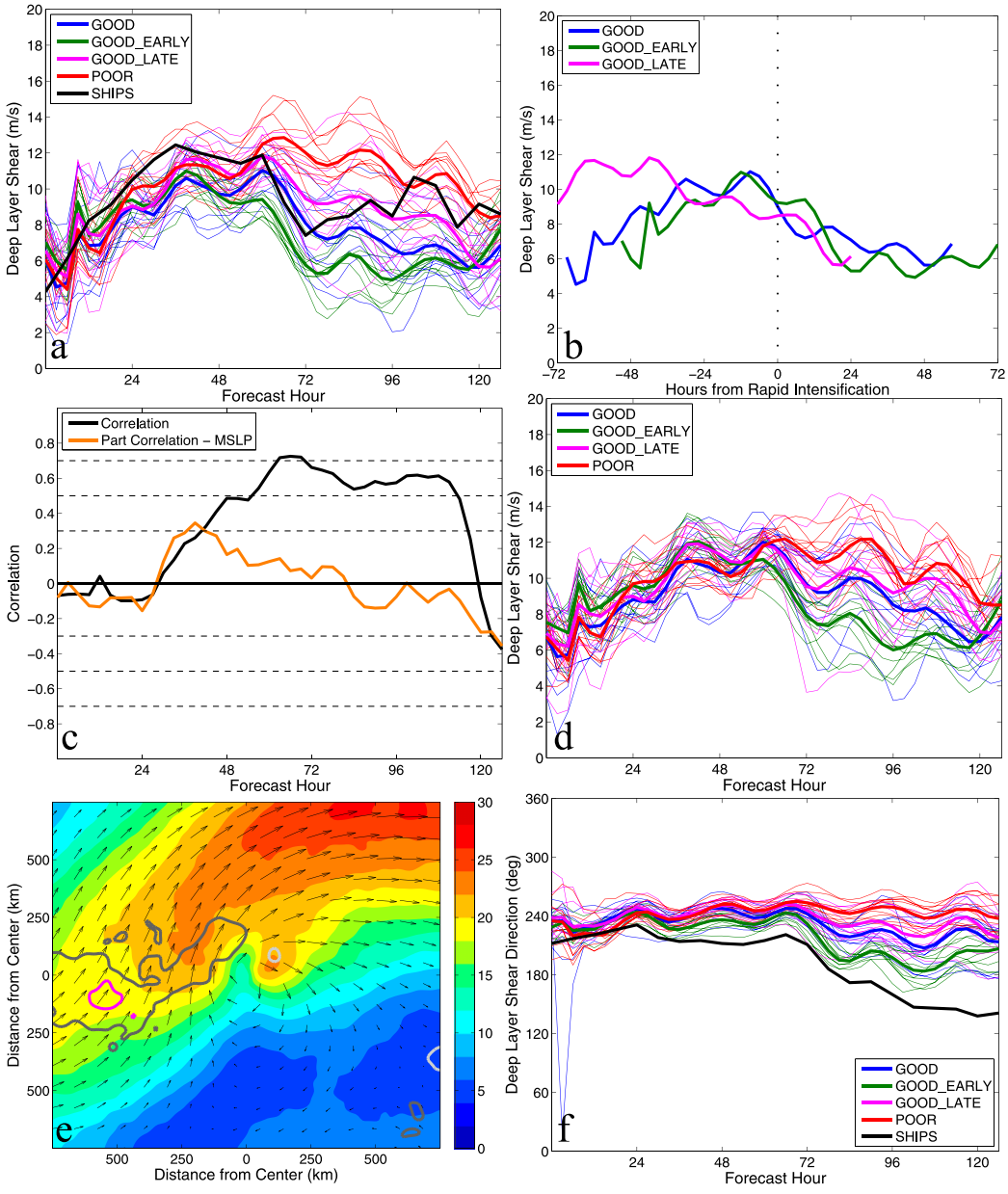

FIG. 6. (a) Evolution of the magnitude (m s^{-1}) of deep-layer (850–200 hPa; averaged over a 200–800-km annulus) wind shear for the mean (thick) and the individual ensemble members (thin) of the composite groups GOOD (blue), GOOD_EARLY (green), GOOD_LATE (magenta), and POOR (red). SHIPS (black) deep-layer shear is also plotted. (b) As in (a), but only for the mean of GOOD (blue), GOOD_EARLY (green), and GOOD_LATE (magenta) plotted in relation to the RI-onset time of the composite groups. (c) Evolution of the correlation and part correlation controlling for minimum SLP between deep-layer shear magnitude and RI-onset time calculated from the 30 ensemble members that compose the developing composite groups. (d) As in (a), but for an averaging annulus of 500–800 km from the surface center. (e) Storm-centered horizontal cross section of deep-layer shear (850–200 hPa; contours filled every 2.5 m s^{-1} and vectors) for the members of the composite groups at 0000 UTC 13 Sep 2014 (36 h) overlaid with spatial part correlation (controlling for minimum SLP) contours between the shear magnitude and RI-onset time (+0.3 in dark gray, +0.5 in magenta, −0.3 in light gray, and −0.5 in white). (f) As in (a), but for direction (°).

simulations of Tao and Zhang (2014) with comparable sea surface temperatures (~29°C; Fig. 1a).

Examining shear in a timeframe relative to the RI-onset time of each composite group (Fig. 6b) reveals some striking similarities between the composites. In this framework, it is clear that the shear magnitude in the developing composites begins to decrease at least ~6–12 h prior to RI. The decrease in shear in GOOD_LATE begins even earlier (~36 h prior to RI), although the peak magnitude of shear was stronger than the other developing composites so that a greater decrease in shear was necessary prior to RI. In addition, the shear magnitude of all composites at RI is very similar (~8–9 $m\,s^{-1}$). Over the final 2–3 days of the simulation, the shear magnitudes for the developing composite groups decrease steadily to a moderate value of ~7 $m\,s^{-1}$.

A correlation analysis further demonstrates that shear delays RI-onset in some of the composites. Figure 6c shows both the correlation and part correlation[3] between the deep-layer shear magnitude and the RI-onset time calculated from the 30 members that compose the composite groups that undergo RI. Although the correlation is insignificant throughout the first 24 h of the simulation, a significant positive correlation begins to develop over the next 24–48 h. The correlation is moderate (~0.5) by 48 h, and it becomes strong (~0.8) by 72 h as the majority of the members approach RI onset. Meanwhile, the part correlation between shear magnitude and RI-onset time (while controlling for minimum SLP) has a similar evolution to the correlation over the first 36 h. However, the part correlation peaks at 36 h, suggesting a brief window of time when shear is an independent cause of RI timing differences. This time window corresponds to the time when shear in GOOD_EARLY and GOOD decreases to values slightly lower than those in GOOD_LATE. Meanwhile, the correlation and part correlation begin to diverge by 48 h, when shear differences become as much an effect of intensity differences as a cause of them.

While a decrease in deep-layer shear can sometimes be the result of vortex alignment (e.g., if alignment is forced by a change in inner-core convection rather than a change in shear), results here suggest that much of the change in shear here is supplied by the environment. This is shown by calculating a more ''environmental'' deep-layer shear, which is area averaged from 500 to 800 km in Fig. 6d. The environmental shear steadily increases in all composite groups throughout the first 48 h of the simulation, but a similar separation in shear magnitude develops as in Fig. 6a. The environmental shear in GOOD_EARLY is lower than that in the other composites after 60 h, and at around the same time the shear in GOOD and GOOD_LATE becomes lower than that in POOR. Between 72 and 96 h, the shear in GOOD becomes lower than that in GOOD_LATE and POOR. These differences again suggest that a significant environmental component contributes to the RI-onset variability.

The variability in shear that leads to differences in RI onset appears to be related to a band of higher shear that Edouard moves into. To show this more clearly, Fig. 6e overlays a composite of shear at 36 h with the part correlation between shear magnitude and RI-onset time (controlling for minimum SLP). The resulting correlation shows that RI occurs earlier when shear in the south edge of the band, on the north and west sides of Edouard, is lower. A similar pattern of part correlation is evident at 48 h (not shown) even as the part correlation between area-average shear and RI-onset time decreases.

The evolution of deep-layer shear direction (Fig. 6f) also appears to be somewhat related to RI-onset time. Initially southwesterly (~240°), the shear direction is comparable among all composite groups through 48–72 h. However, over the next 2 days of the simulation, the directions of the shear vectors begin to diverge as the shear vectors of the members that achieve RI earlier rotate counterclockwise more significantly toward a southeasterly orientation. In addition, the direction of the shear vectors of the nondeveloping members (POOR) does not change significantly throughout the majority of the simulation. The precession process that the developing vortices are undergoing throughout this period likely contributes to these changes in shear direction. It is also possible that, as the TC intensifies, its outflow deforms the upper-tropospheric trough and subsequently changes the shear direction.

Vortex tilt in the composite groups evolves in response to the changing shear. Figure 7a shows the mean tilt magnitudes for each composite group, which are defined as the distance between the 850- and 500-hPa weighted horizontal circulation centers as in Zhang and Tao (2013). The tilt magnitudes of all composite groups are initially similar (~30–40-km) and all steadily increase throughout the first 24 h of the simulation, coinciding with the increase in deep-layer shear. Over the next 24 h, the GOOD_EARLY tilt magnitude begins to gradually decrease, while the tilt in the other composites continues to increase. The mean tilt of the GOOD

[3] Part correlation analyses are used to clarify relationships when multiple variables are correlated with each other. The first-order part correlation between two variables while controlling for a third variable effectively treats the third as a constant (e.g., Sippel et al. 2011).

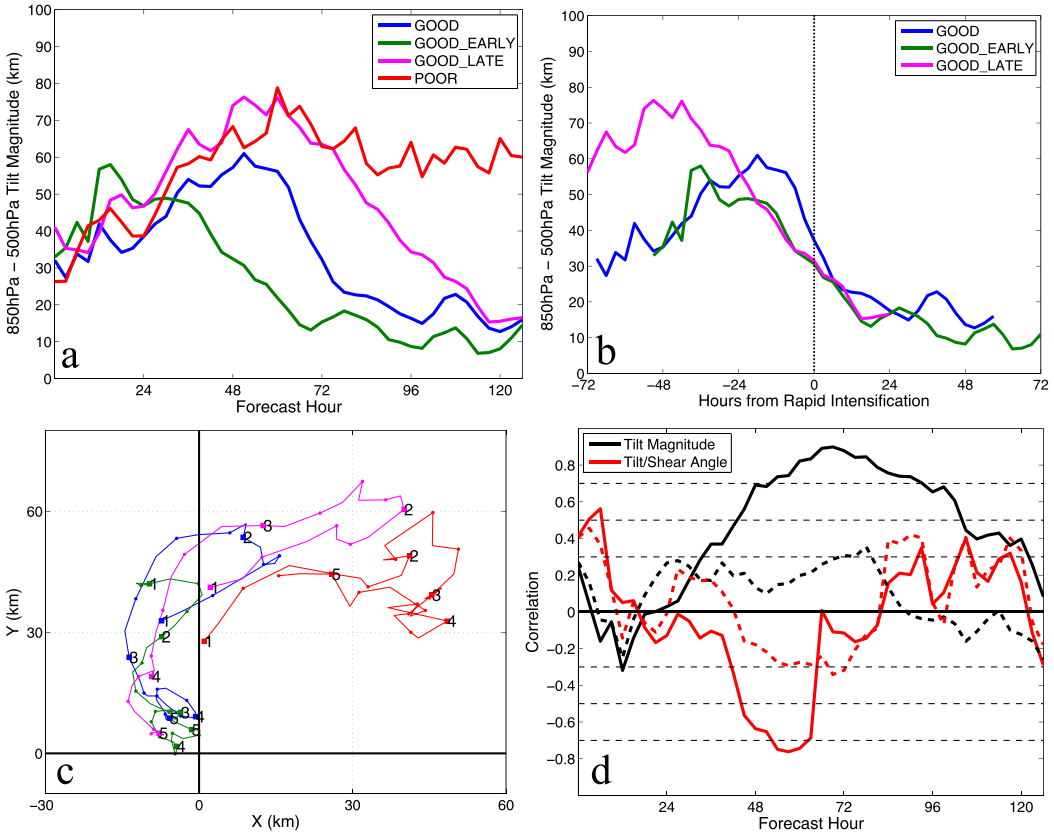

FIG. 7. (a) Evolution of the mean tilt magnitude (distance between weighted horizontal circulation centers at 850 and 500 hPa; km) for the composite groups GOOD (blue), GOOD_EARLY (green), GOOD_LATE (magenta), and POOR (red). (b) As in (a), but only for the composites that undergo RI, shown in relation to RI-onset time. (c) Tilt vector evolution starting at 24 h for GOOD (blue), GOOD_EARLY (green), GOOD_LATE (magenta), and POOR (red) with positions marked every 6 h (dots) and every 24 h (squares with simulation day indicated). (d) Evolution of the correlation between RI onset and the tilt magnitude (black) as well as the angle between the tilt and deep-layer shear vector (red). Correlation is calculated using the 30 members of the developing composite groups. Dashed lines indicate part correlation controlling for minimum SLP between RI onset and tilt magnitude (dashed black) and RI onset and the tilt/shear angle (dashed red).

vortices starts to decrease at ~48 h, the mean tilt of the GOOD_LATE vortices decreases at ~60 h, and the mean tilt magnitude of POOR stops increasing at 48 h and remains relatively constant throughout the rest of the simulation. The developing composite tilt magnitudes continue to decrease as the storms intensify, and by the end of the simulation all three developed composites have tilt magnitudes of ~15 km. The GOOD_EARLY simulation exhibits somewhat different behavior than the others since its tilt begins to decrease at the same time that its shear is relatively high. The shear in GOOD_EARLY is roughly the same as that in GOOD and GOOD_LATE through about 36 h, and it is not notably lower than that in GOOD until after 48 h. Meanwhile, vortex tilt in GOOD_EARLY begins to decrease markedly at 36 h in spite of the relatively high shear. This evolution suggests that the initially stronger vortex in GOOD_EARLY very likely helps it to resist the shear and more readily achieve vortex alignment.

The results here also suggest that the vortices follow a very similar pathway toward intensification despite differences in timing and, furthermore, that the vortices will not undergo RI until alignment has essentially occurred. For example, the tilt evolution is analyzed in relation to the RI times in the composites in Fig. 7b, where it is clear that the tilt magnitude begins to decrease ~24–48 h prior to RI-onset in all developing composites. In addition, despite some discrepancy among the composites in the magnitude of the maximum tilt, the tilt magnitudes at the time of RI are ~30–40 km.

The time evolution of the tilt vectors reveals that only the composites that precess into the upshear quadrant are able to achieve RI, and the composites embedded in

stronger shear develop larger tilt magnitudes and have longer vortex precession and delayed RI onset. To demonstrate this, Fig. 7c shows the mean evolution of the tilt vectors from the composite groups in an Earth-relative x–y plane from 24 h to the end of the simulation. It is clear that the increasing shear over the first 24–48 h of the simulation causes the tilt vectors of the composite groups to be oriented in the downshear direction (toward the northeast), which is consistent with the observed tilt of Edouard (Braun et al. 2016). By 48 h, as the shear magnitude and direction begins to diverge among the composites, the orientation and magnitude of the tilt diverges as well. The GOOD_EARLY tilt vector has a smaller magnitude and is oriented farther to the northwest at this time, indicating that the members of this group are further along in their precession process and closer to alignment and RI onset. By 72 h, the GOOD vortices are also completing precession and beginning RI, while the GOOD_LATE tilt vectors are continuing to rotate counterclockwise toward the upshear quadrant. Meanwhile, the POOR tilt vectors have the largest magnitudes (under the strongest shear conditions) and remain in the downshear quadrant throughout the simulation.

The correlation between the tilt magnitude and RI onset quantitatively demonstrates the impact of vortex tilt on RI onset time (Fig. 7d). Over the first 24 h of the simulation, the correlation is insignificant as the ensemble members have comparable tilt under the steadily increasing shear. However, by 36 h the correlation is significant with 95% confidence (~0.3), and by 48 h it is moderate (~0.5), suggesting that decreasing tilt magnitude leads to earlier RI onset. The part correlation between tilt magnitude and RI-onset time (again controlling for minimum SLP) confirms the relationship (Fig. 7d). Curiously, the part correlation does not peak until 72–84 h, suggesting a long-lasting impact from the earlier shear.

Previous studies have shown that it is difficult for a developing TC vortex to achieve RI until the tilt vector precesses into the upshear quadrant (Frank and Ritchie 2001; Braun et al. 2006; Braun and Wu 2007; Tao and Zhang 2014, 2015; Rogers et al. 2015), so Fig. 7d also shows the correlation and part correlation between the RI-onset time and the shear-relative tilt angle. Tilt angle here is defined as the difference in direction between the tilt and shear vectors with a discontinuity at 180° to obtain a more representative correlation. The correlation is insignificant over the first 24 h, but it steadily increases through 72 h to a strong value of ~−0.7, indicating that RI onset is strongly related to differences in the direction of the tilt and shear vectors. The part correlation controlling for current intensity (i.e., minimum SLP) confirms the tilt vector as being an independent factor contributing to RI delay. Similar to the relationship between RI onset and tilt magnitude, the part correlation between RI onset and the tilt angle peaks around 72 h. This again suggests a long-lasting impact of the earlier shear. After 72 h, the part correlation becomes very noisy, a result of the fact that the majority of the members are aligned or nearly aligned.

Because the interaction between TC vortices and shear is intimately related to the distribution of convection, the impacts of shear on the strength and location of the developing convection is investigated next. Figure 8 shows the storm-centered composite maximum radar reflectivity, minimum SLP, 10-m surface winds, deep-layer shear vector, and tilt vector evolutions for GOOD_EARLY, GOOD, GOOD_LATE, and POOR. The composites indicate that the storms are initially somewhat asymmetric, with the majority of the strongest convection located to the north and west of the storm center. By 24 h, as the shear magnitude increases and the vortices become increasingly tilted toward the north (downshear left), the areal coverage of convection is reduced, with the strongest convection located primarily in the downtilt direction. Also, by this time, the inner-core convection associated with GOOD_EARLY is stronger (Fig. 8), which probably contributes to an earlier alignment and RI onset. At 48 h, GOOD_EARLY has essentially aligned with inner-core convection wrapped around the surface circulation, while the strength of the GOOD and GOOD_LATE convection has increased. The POOR convection remains somewhat weaker in the inner core and is aligned strictly in the downshear direction.

Recent work from Rogers et al. (2016) has shown that RI is associated with an increase in upshear-left convection, which is also found in the composites here. The change in convective distribution is illustrated with contoured frequency by altitude diagrams (CFADs; Fig. 9) of inner-core (within 50 km of the surface center) upshear-left radar reflectivity (dBZ) from 24 to 48 h. As discussed above, RI onset typically does not occur until the tilt vector precesses into the upshear-left quadrant, and the same holds true regarding the convection. The CFADs clearly demonstrate that significant convection is already present in this quadrant (Figs. 9a,e) in GOOD_EARLY, foretelling its imminent RI. However, convection in GOOD, GOOD_LATE, and POOR is significantly weaker and sparser. Note that by 36–48 h the upshear-left convection in GOOD (Fig. 9f) is slightly stronger than in either GOOD_LATE (Fig. 9g) or POOR (Fig. 9h), which may help accelerate precession. It is also likely that weaker shear in GOOD promotes stronger inner-core upshear-left convection and contributes to an earlier RI onset.

The remaining composite simulations have similar interactions between shear, tilt, and convection. By 72 h,

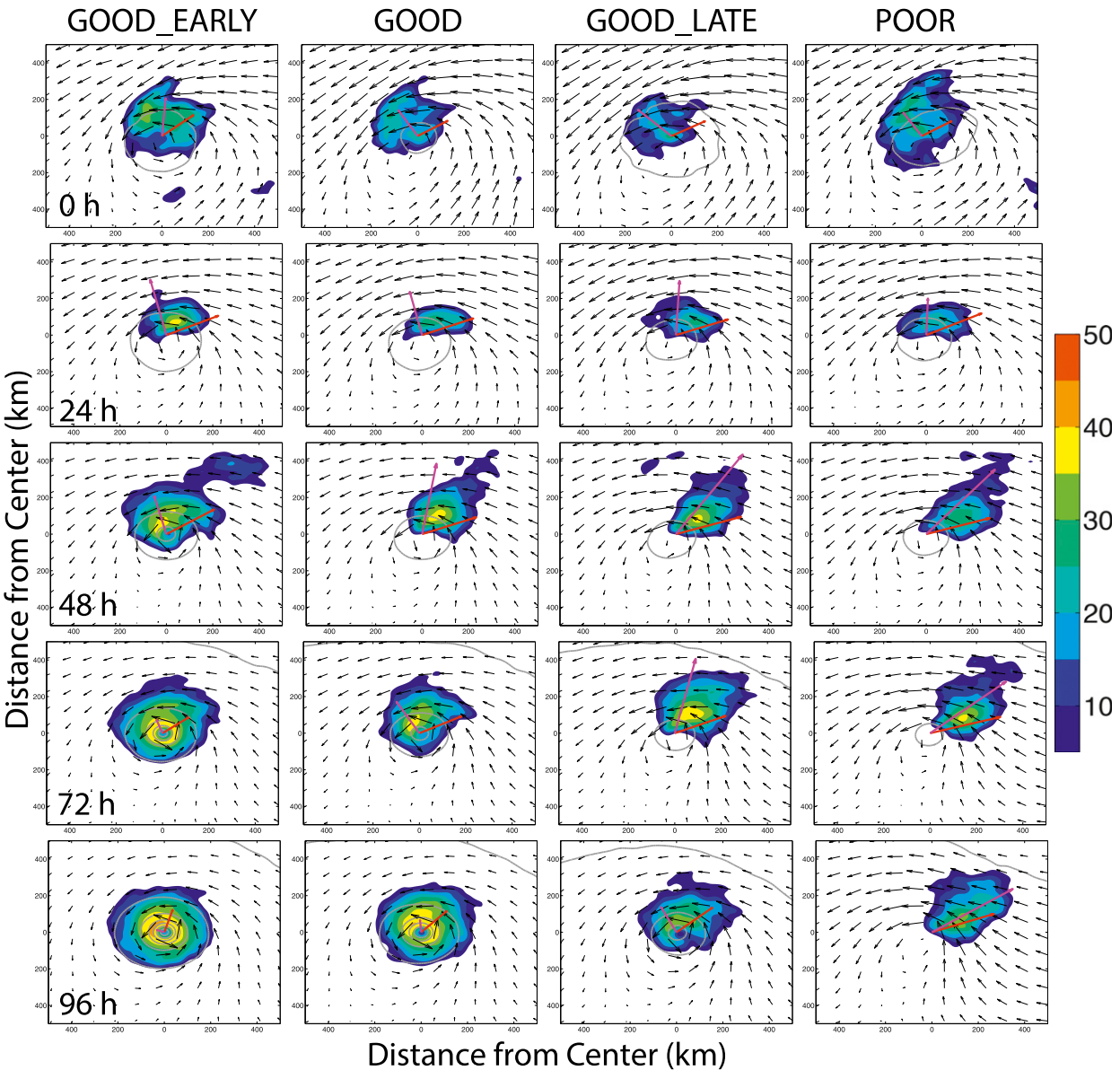

FIG. 8. Surface maps of storm-centered composite maximum simulated radar reflectivity (filled contours every 5 dBZ, beginning at 5 dBZ), minimum SLP (gray contour lines every 10 hPa), and 10-m winds (vectors) for the (left)–(right) GOOD_EARLY, GOOD, GOOD_LATE, and POOR composite groups at (top)–(bottom) 0, 24, 48, 72, and 96 h for a portion of the 9-km inner domain in the forecast system. Composite deep-layer (850–200 hPa) shear vectors (red) and 850–500-hPa vortex tilt vectors (magenta) originate from the composite surface center. The minimum SLP contours and the surface wind vectors have been smoothed (using a 1–2–1 smoother in both the x and y directions) 10 times for clearer visualization. To assist the reader, it should be noted that, in each panel, the tilt vector is oriented to the left of the shear vector.

the inner-core convection in GOOD has also wrapped around the surface center as RI is commencing, while the regions of strongest convection in GOOD_LATE have begun to rotate counterclockwise as the precession of the tilt vector has proceeded. The convection associated with POOR at this time has also increased in strength, but the strong shear keeps it primarily in the downshear-left quadrant, and the tilt vector cannot precess in the upshear direction. Finally, GOOD_LATE approaches alignment by 96 h, while the POOR convection remains downshear and embedded in less favorable environmental conditions. It is possible that, given more time and sufficiently low shear, storms in POOR would align and undergo RI.

Radar reflectivity composites evaluated in relation to the time before RI (Fig. 10), reveal that the vortices and

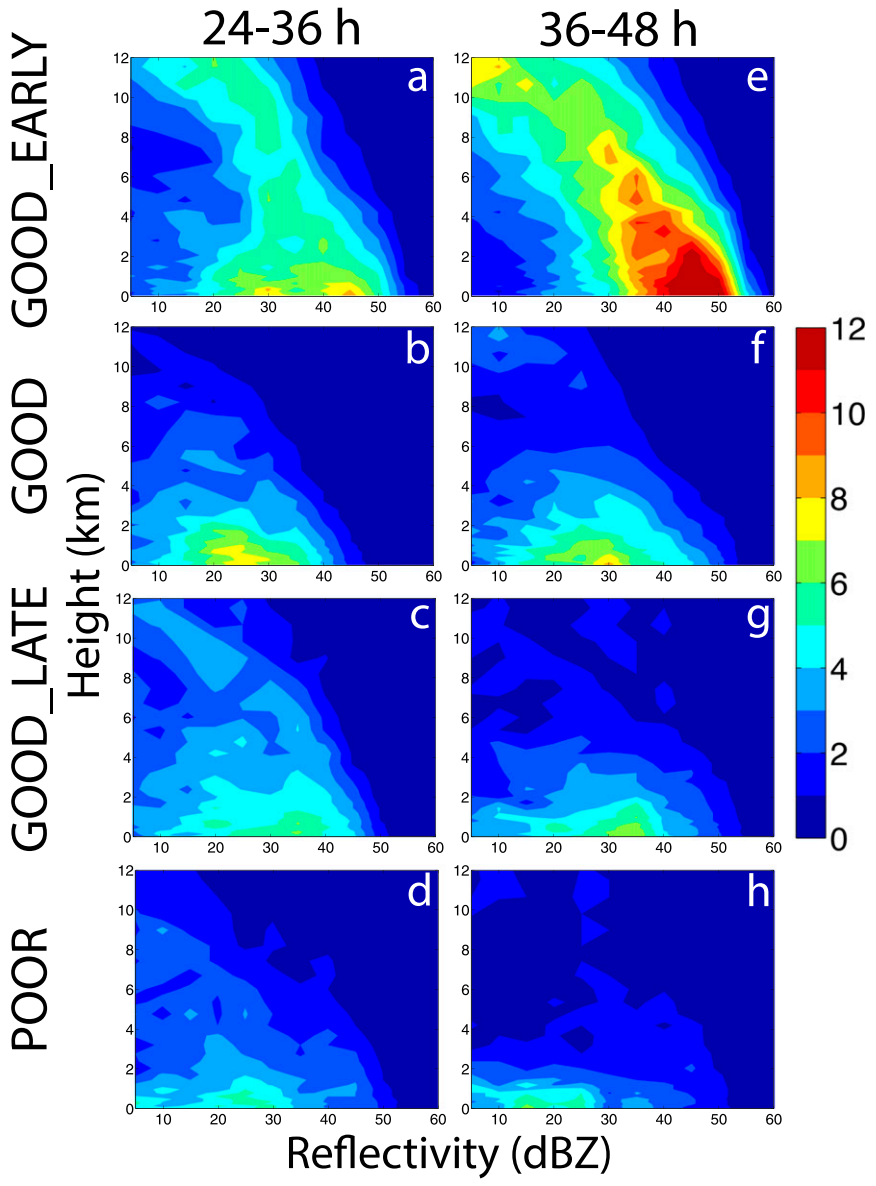

FIG. 9. Composite contoured frequency (raw counts) by altitude (km) diagrams for radar reflectivity (dBZ) in the upshear-left quadrant within 50-km of the surface center for the (a) GOOD_EARLY, (b) GOOD, (c) GOOD_LATE, and (d) POOR composite groups for 24–36 h. (e)–(h) As in (a)–(d), respectively, but for 36–48 h.

their associated convection follow similar pathways to RI. From this perspective it is clear that, although there is significant variability among the composites in the areal coverage and the strength of the convection 48 h prior to RI, as RI onset is approached, substantial parallels in both the position and strength of the convection and the magnitude and orientation of the tilt vector exist. Despite some differences in the tilt orientation at 24 h prior to RI, the tilt vector and convection in the composites for the most part rotate counterclockwise. By 12 h prior to RI the inner-core convection has strengthened, particularly in GOOD_EARLY and GOOD. By the time of RI, the tilt/shear angle is ~60°–90° across the composites, and convection has wrapped around the surface circulation. This analysis further demonstrates that, despite differences in RI timing, the developing vortices undergo a similar evolution as RI is approached.

e. Ensemble sensitivity to RI onset: Initial conditions

The sensitivity of the RI-onset times to the initial conditions is investigated next by creating simulations

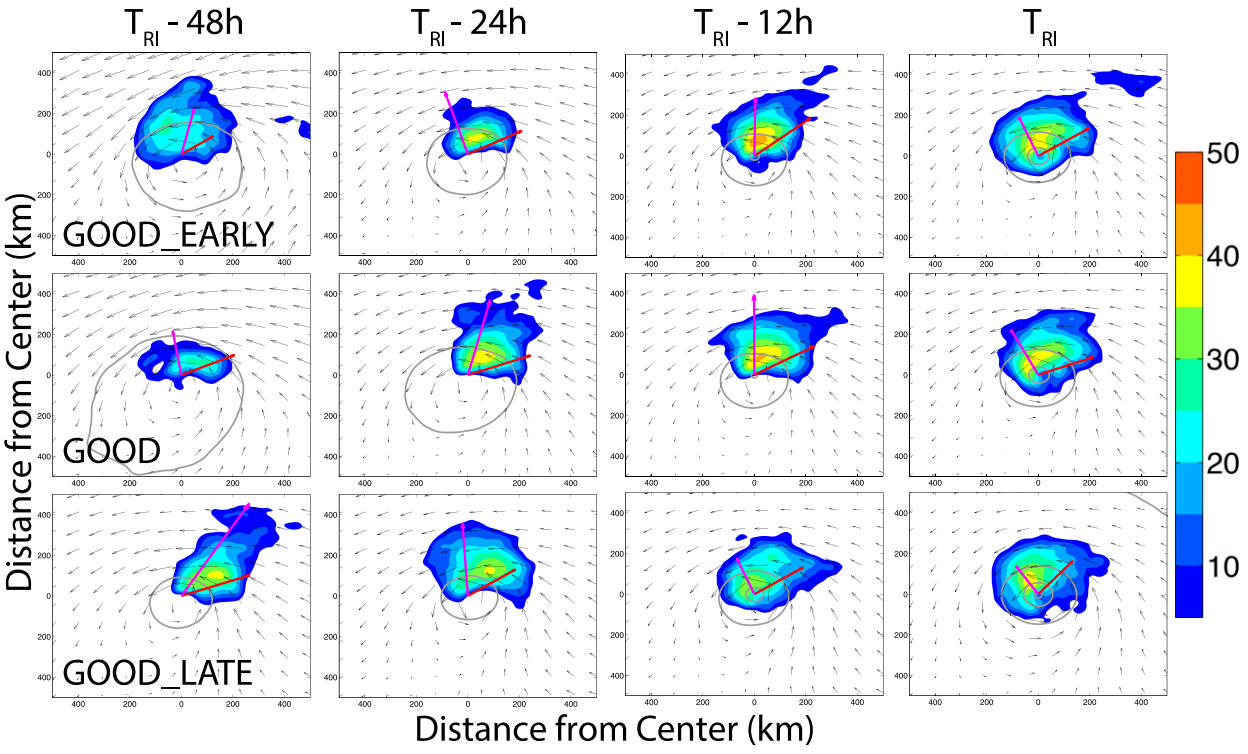

FIG. 10. As in Fig. 8, but composites [(top) GOOD_EARLY, (middle) GOOD, and (bottom) GOOD_LATE] shown in relation to RI-onset time.

initialized with composite initial conditions from the GOOD_EARLY, GOOD, GOOD_LATE, and POOR groups (refer to section 2c for additional details). The tracks, minimum SLP, and maximum 10-m winds of these simulations are shown in Fig. 11. Both the GOOD_EARLY and POOR composite simulations show similar behavior to that of the original ensemble means, with the GOOD_EARLY simulation undergoing RI at ~48 h and the POOR simulation not significantly intensifying throughout the simulation window. The tracks in the composited simulations are also quite similar to those in the original ensembles (Fig. 11a), with the exception of POOR, which takes a more northwestward track as the TC begins to intensify near the end of the simulation.

The intensity evolutions of the GOOD and GOOD_LATE simulations converge to a solution with an RI-onset time of approximately that of GOOD from the original ensemble (Figs. 11b,c). Although there is ~24–36 h between RI for GOOD and GOOD_LATE members in the original ensemble, the GOOD and GOOD_LATE simulations initialized from the composite initial conditions cannot be compared to further explore Edouard's predictability. Therefore, in all remaining sensitivity experiments, GOOD_LATE will not be discussed.

To test the hypothesis that the GOOD_EARLY vortices undergo RI prior to the rest of the ensemble because they are initially stronger, additional sensitivity experiments are performed utilizing the composited initial conditions from GOOD_EARLY, GOOD, and POOR. Two experiments (EnvGoodEarlyTcGood and EnvGoodEarlyTcPoor) are created by replacing the near-storm (<200 km) initial conditions of GOOD_EARLY with the initial conditions from GOOD and POOR (refer to section 2c and Table 1 for a description of how this was done and of the naming convention for the subsequent sensitivity experiments). The tracks (Fig. 12a), minimum SLP (Fig. 12b), and maximum 10-m winds (Fig. 12c) from EnvGoodEarlyTcGood and EnvGoodEarlyTcPoor are shown in Fig. 12. Storm intensity in these two simulations is similar to that in the GOOD simulation, and RI begins around 72 h. This demonstrates that the insertion of the initially weaker inner core of the GOOD or POOR vortex in the GOOD_EARLY environment leads to a delay in RI onset of about 24 h, providing more evidence that the initially stronger GOOD_EARLY vortex significantly contributes to the earlier RI.

The intensity evolutions of the complimentary experiments EnvGoodTcGoodEarly and EnvPoorTcGoodEarly are also shown in Fig. 12. Both the minimum SLP

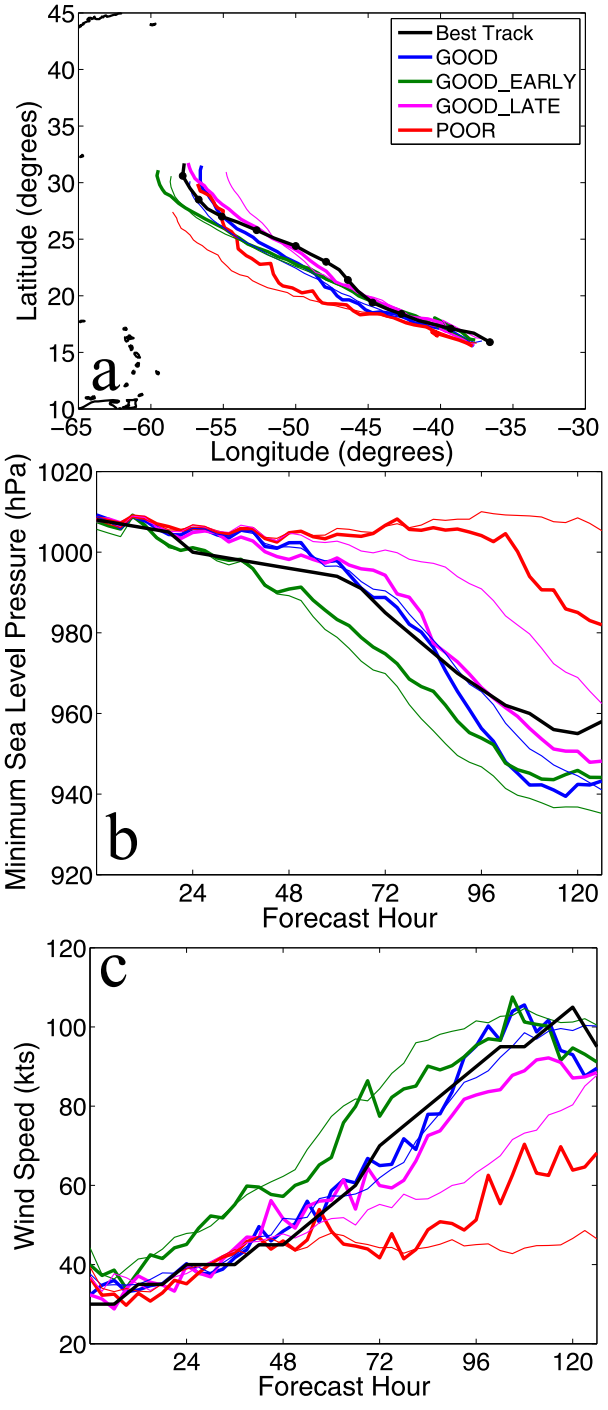

FIG. 11. (a) Tracks, (b) minimum SLP (hPa), and (c) maximum 10-m wind speed (kt) for the composited initial-condition sensitivity experiment [thick; GOOD (blue), GOOD_EARLY (green), GOOD_LATE (magenta), and POOR (red)] and the composite group means from the original ensemble (thin). NHC best track is in black [positions marked every 12 h in (a)].

(Fig. 12e) and maximum 10-m winds (Fig. 12f) of the EnvGoodTcGoodEarly experiment indicate that this simulation undergoes RI at 48 h, which is the time of RI onset of GOOD_EARLY. This result shows that the initially stronger GOOD_EARLY vortex is not particularly sensitive to small degradations of its initial environment. Meanwhile, RI in EnvPoorTcGoodEarly begins at 72 h, as in the GOOD composite, indicating that the environment in POOR is not conducive for intensification, to the extent that it delays RI of even initially strong vortices.

Additional composites are created to test the hypothesis that the POOR environment is detrimental to intensification (EnvGoodTcPoor and EnvPoorTcGood). The minimum SLP (Fig. 13b) and maximum 10-m wind (Fig. 13c) evolutions from this set of sensitivity experiments reveal that EnvGoodTcPoor undergoes RI at ~72 h, as in GOOD, while EnvPoorTcGood does not begin to intensify until near the end of the simulation, as in POOR. Given the comparable initial strengths of the GOOD and POOR vortices, these results strongly suggest that the POOR environment is less favorable for development in this ensemble.

Next, we seek to identify the radius from the storm center near which adverse environmental conditions begin to occur in POOR through sensitivity experiments initialized with linearly combined GOOD and POOR composited initial conditions at varying radii (Table 1). The EnvPoorTcGood650 experiment fails to develop until near the end of the simulation, while EnvGoodTcPoor650 has an RI-onset time of ~72 h. Meanwhile, EnvPoorTcGood1100 begins RI just after 72 h, while the EnvGoodTcPoor1100 experiment intensifies considerably later in the simulation (Figs. 13b,c). These intensity evolutions demonstrate that the region in the POOR environment possessing conditions unfavorable for RI lies between 650 and 1100 km from the center of Edouard.

More systematic sensitivity experiments in which the radius at which the GOOD and POOR composites are combined is incrementally increased from 500 to 900 km (Table 1) reveal that the region of greatest sensitivity to RI in the POOR environment is between 800 and 900 km. EnvGoodTcPoor800 undergoes RI, while EnvGoodTcPoor900 does not. In addition, the opposite experiments exhibit the opposite behavior; EnvPoorTcGood800 does not intensify, while EnvPoorTcGood900 has an RI-onset time of ~72 h. The environmental influences in this narrow region of POOR that are inhibiting RI are explored in detail in the next section.

f. Ensemble sensitivity to RI onset: Assessing adverse conditions in the POOR environment

Before investigating in greater detail the unfavorable environmental influences in the sensitive region in the

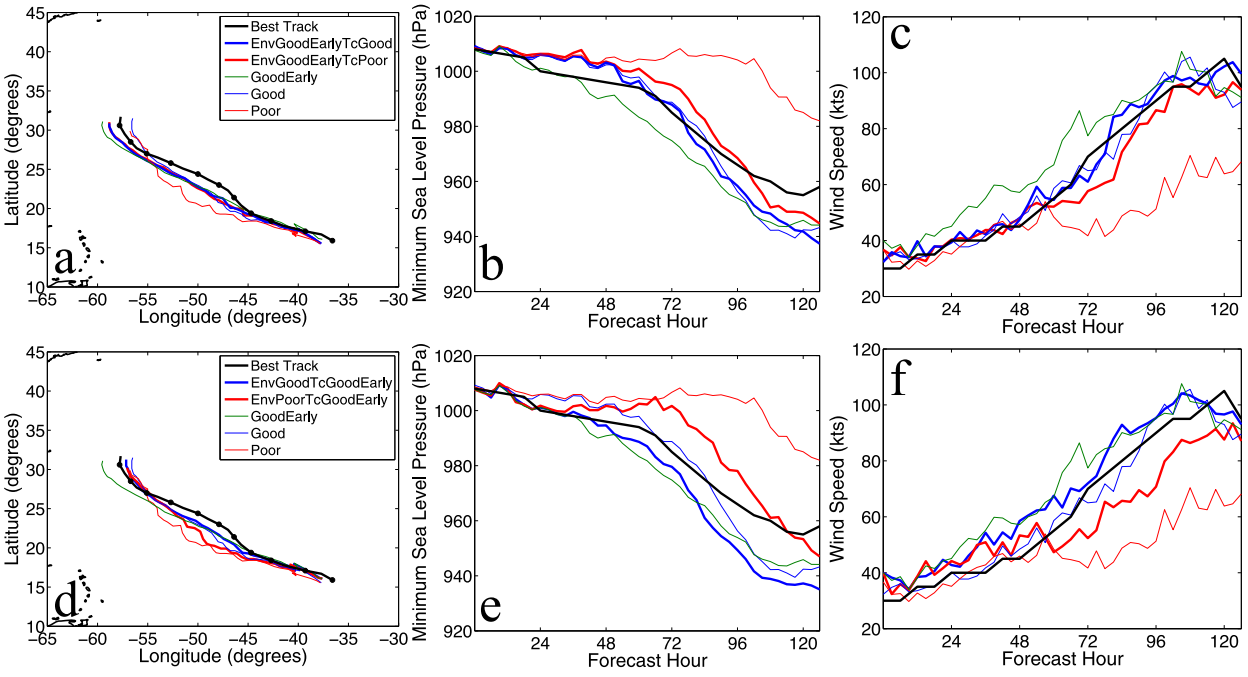

FIG. 12. (a) Tracks, (b) minimum SLP (hPa), and (c) maximum 10-m wind speed (kt) evolution for the sensitivity experiment in which the initial vortex in the GOOD_EARLY composite is replaced by that of GOOD (EnvGoodEarlyTcGood; thick blue) and POOR (EnvGoodEarlyTcPoor; thick red). Results from the composited initial-condition sensitivity experiment [GOOD_EARLY (thin green), GOOD (thin blue), and POOR (thin red)] and NHC best track [black; positions marked every 12 h in (a)] are also included. (d)–(f) As in (a)–(c), respectively, but for the sensitivity experiment in which the GOOD_EARLY vortex is placed in the GOOD (EnvGoodTcGoodEarly; thick blue) and POOR (EnvPoorTcGoodEarly; thick red) environment.

POOR composite, the very subtle differences in this highly sensitive region of this ensemble should first be highlighted. An example of the magnitude of these differences is shown in Fig. 14a, which contains vertical profiles of the RMSDs in zonal wind, meridional wind, temperature, and specific humidity between EnvGoodTcPoor800 and EnvGoodTcPoor900 in the sensitive region (between 800 and 900 km from the surface center). The differences in both the zonal and meridional winds are $\sim$0.5 m s^{-1} throughout the profile, which is comparable to the accuracy of the dropsondes used in HS3. The RMSDs in the temperature and specific humidity profiles peak near the top of the boundary layer at $\sim$0.2 K and 0.35 g kg^{-1}, respectively, with both gradually decreasing in magnitude with altitude. These differences in the thermodynamic variables are also at or below the levels of accuracy obtained by the HS3 dropsondes. This finding demonstrates that, although it is evident that the POOR environment has detrimental impacts on RI, there is a very specific region of the environment in which differences smaller than the observable dropsonde errors can determine whether the simulation will undergo RI. This suggests that at times it will likely be impossible to determine operationally whether RI was going to occur with certainty.

Given the fact that the area of sensitivity in the POOR environment is at a large distance from the surface center of Edouard, it is hypothesized that the factor impeding RI is dry environmental air (Fig. 3a) that is subsequently advected toward the TC circulation. To test this, the moisture fields in the initial conditions from EnvGoodTcPoor800 are modified in the region of greatest sensitivity (between 700 and 900 km; EnvGoodTcPoor800DiffQ). Examples of the differences between the experiments that result from the modifications to the moisture fields are shown in the initial 800- and 500-hPa relative humidity fields (Figs. 14b,c). As by design, the two initial conditions only differ in the 700–900-km region, and these differences are very small (at most 4%–6% relative humidity and an RMSD of 0.6 g kg^{-1} in specific humidity near the top of the boundary layer; Fig. 14a).

Despite these very small differences in only the moisture fields of the initial conditions, EnvGoodTcPoor800 undergoes RI at $\sim$72 h while EnvGoodTcPoor800DiffQ does not begin to intensify until near the end of the 5-day simulation window (not shown). A comparison of the maximum radar reflectivity fields of the experiments reveals that, over the first $\sim$48 h of the simulations, the evolution of the location and strength of

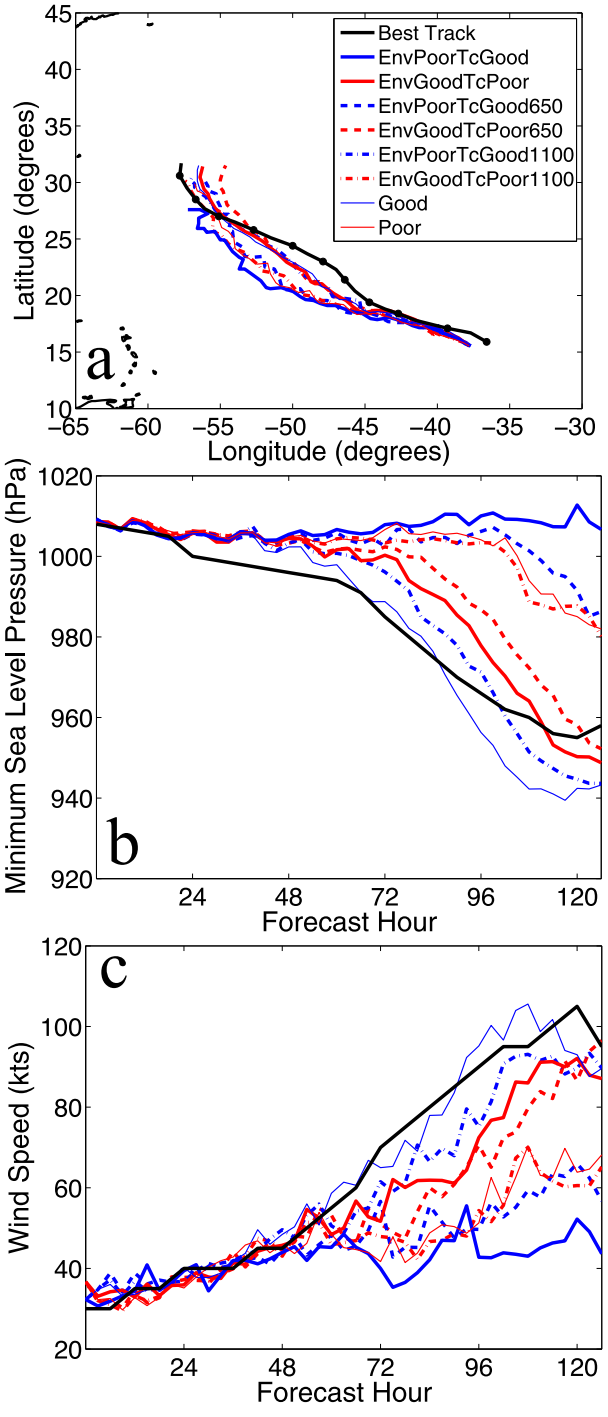

FIG. 13. (a) Track, (b) minimum SLP (hPa), and (c) maximum 10-m wind speed (kt) evolution for the sensitivity experiments that replace the initial vortex in the GOOD composite with that of POOR (EnvGoodTcPoor; red) and vice versa (EnvPoorTcGood; blue). The experiments vary according to the radius at which the composites are blended [200–300 km (solid), 500–800 km (650) (dashed), and 1000–1200 km (1100) (dashed–dotted)]. The NHC best track [black; positions marked every 12 h in (a)] and the composite initial-condition sensitivity experiments [GOOD (thin blue); POOR (thin red)] are also included.

convection is essentially identical (not shown). A demonstration of the substantial resemblance in storm structure over the first half of the experiments is in Figs. 15a and 15d, which shows the maximum radar reflectivity, minimum SLP, 10-m surface winds, shear vector, and tilt vector at 51 h for EnvGoodTcPoor800 and EnvGoodTcPoor800DiffQ. These reflectivity fields represent the first time at which any visible differences can be detected between the experiments, and these differences are minor. At this time, the inner-core convection to the northeast of the surface center appears to be stronger in EnvGoodTcPoor800 than in EnvGoodTcPoor800DiffQ. Most likely as a result of this stronger burst of convection, the tilt vector is oriented more toward the north in EnvGoodTcPoor800 as the precession process has begun to accelerate.

A result of the difference in the strength of the convective bursts can be seen in the 985-hPa θ_e at 51 h, where there is a stronger surface cold pool associated with the inner-core convection in EnvGoodTcPoor800 (Figs. 15c,f). The near-surface θ_e also reveals the slight difference in position of the convective burst between the two simulations. In EnvGoodTcPoor800, the inner-core convection and the associated tilt vector have rotated farther in the counterclockwise direction than in EnvGoodTcPoor800DiffQ, which appears to have helped quicken the precession process and allow RI to more easily occur. These differences in inner-core convective strength can also be seen in the evolution of the maximum radar reflectivity (dBZ) frequencies (area averaged within 150 km of the surface center) for the EnvGoodTcPoor800 (Fig. 15g) and EnvGoodTcPoor800DiffQ (Fig. 15h) experiments. The differences between these two frequency diagrams (Fig. 15i) suggest that there is some signal of stronger inner-core convection in EnvGoodTcPoor800 at approximately 42 h; however, a stronger signal appears at 51 h (coinciding with Figs. 15a and 15d), in which the strongest reflectivity values occur more frequently in the convection associated with EnvGoodTcPoor800, which subsequently facilitates the intensity divergence.

Differences in inner-core convection result in clear divergence in storm structure as RI is beginning in EnvGoodTcPoor800, as shown in the maximum radar reflectivity fields at 84 h (Figs. 15b,e) and the differences in the reflectivity frequencies (Fig. 15i). At RI onset in EnvGoodTcPoor800, the angle between the tilt and shear vectors has approached 90°, and convection has begun to wrap around the inner core. Meanwhile, the tilt vector and the regions of strongest convection in EnvGoodTcPoor800DiffQ remain in the downshear quadrant. RI is still possible in this simulation, as the vortex appears to be slowly precessing toward the upshear quadrant; however, significant intensification does not occur in the simulation window. These results show that

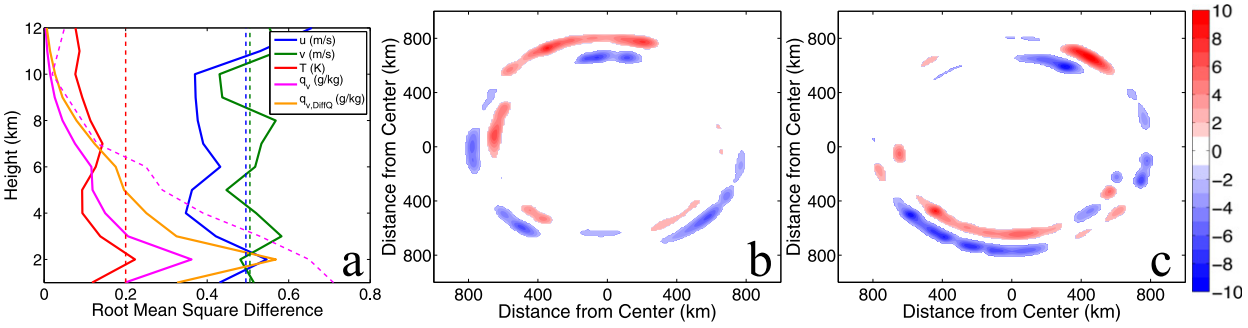

FIG. 14. (a) Vertical profiles of the RMSD of zonal wind ($m\,s^{-1}$; blue), meridional wind ($m\,s^{-1}$; green), temperature (K; red), and specific humidity ($g\,kg^{-1}$; magenta) between the experiments with initial conditions that transition from POOR to GOOD at 800 km and those that transition at 900 km. Accuracy of observations for each of the variables as obtained by the AVAPS dropsondes is indicated by the dashed lines (accuracy information from https://www.eol.ucar.edu/instruments/avaps-dropsonde). The RMSD profile of specific humidity between EnvGoodTcPoor800 and EnvGoodTcPoor800DiffQ ($g\,kg^{-1}$; orange) is also included (RMSD between other variables are zero by design in these experiments). Differences (filled contours every 1% between −10% and 10%) between the initial (b) 800- and (c) 500-hPa relative humidity fields of EnvGoodTcPoor800 and EnvGoodTcPoor800DiffQ.

small perturbations in moisture can impact the strength and location of the developing deep convection, which can subsequently lead to differences in precession and therefore RI timing. Given the significant sensitivity present in this ensemble, it should be noted that the addition of similar initial-condition perturbations to other variables (e.g., winds and temperature) could yield similar divergent behavior.

Attempts to diagnose the sources of the difference in the strength of the inner-core convection in EnvGoodTcPoor800 and EnvGoodTcPoor800DiffQ proved to be challenging. We speculate that the small differences between the moisture fields are sufficient to cause divergent behavior in the chaotic interactions of mesoscale features, such as the development of near-surface cold pools that result from moist convection (Zhang and Sippel 2009). Though the Edouard ensemble displays some degree of practical deterministic predictability, since the majority of experiments that use the POOR environment fail to undergo RI, sensitivity experiments in this subsection show that the adverse conditions that prevent RI in the POOR environment may be too subtle to confidently diagnose. This primarily results from the chaotic nature of developing moist convection and is an indication of limited intrinsic predictability. A companion study that utilized additional sensitivity experiments on the same PSU real-time ensemble forecast of Edouard found that the predictability of Edouard's formation and RI can also be impacted by the modulation of moist convection through the diurnal radiation cycle (Tang and Zhang 2016).

4. Summary and conclusions

The governing dynamics and predictability of the rapid intensification of Hurricane Edouard have been explored through the use of a 60-member convection-permitting ensemble and sensitivity experiments generated by the PSU WRF–EnKF hurricane forecast and analysis system. The 5-day forecasts are quite successful, as the deterministic track and intensity forecast closely follows that of the NHC best track record and the majority of the ensemble correctly predicts Edouard's near-RI event. In addition, the representativeness of the forecasted storm structure and surrounding environment of the most successful members compares favorably to AVAPS dropsondes gathered during the 2014 HS3 campaign. Although the majority of the ensemble captures Edouard's intensification, there is considerable variance in the exact timing of RI, with as much as 60 h between the RI onset of the earliest- and latest-developing members.

A number of experiments were conducted to assess the reasons for variability in RI timing in the ensemble. First, groups of members were created according to their RI-onset time (GOOD_EARLY, GOOD, GOOD_LATE, and POOR) in order to test the impacts of various factors on the RI onset. Next, composited initial conditions, which were created by averaging the initial conditions in each group, were used in additional simulations. For each composite, more sets of initial conditions were generated by replacing all fields at all vertical levels within a given radius from the surface center of Edouard with the fields from different sets of composited initial conditions.

An examination of the composite groups demonstrates that the strongest initial vortices have a much quicker path to RI than do the weaker vortices. Despite being embedded in similar shear as vortices in the other composites, they never acquire a large tilt, and they align rather quickly. This suggests that these vortices are more

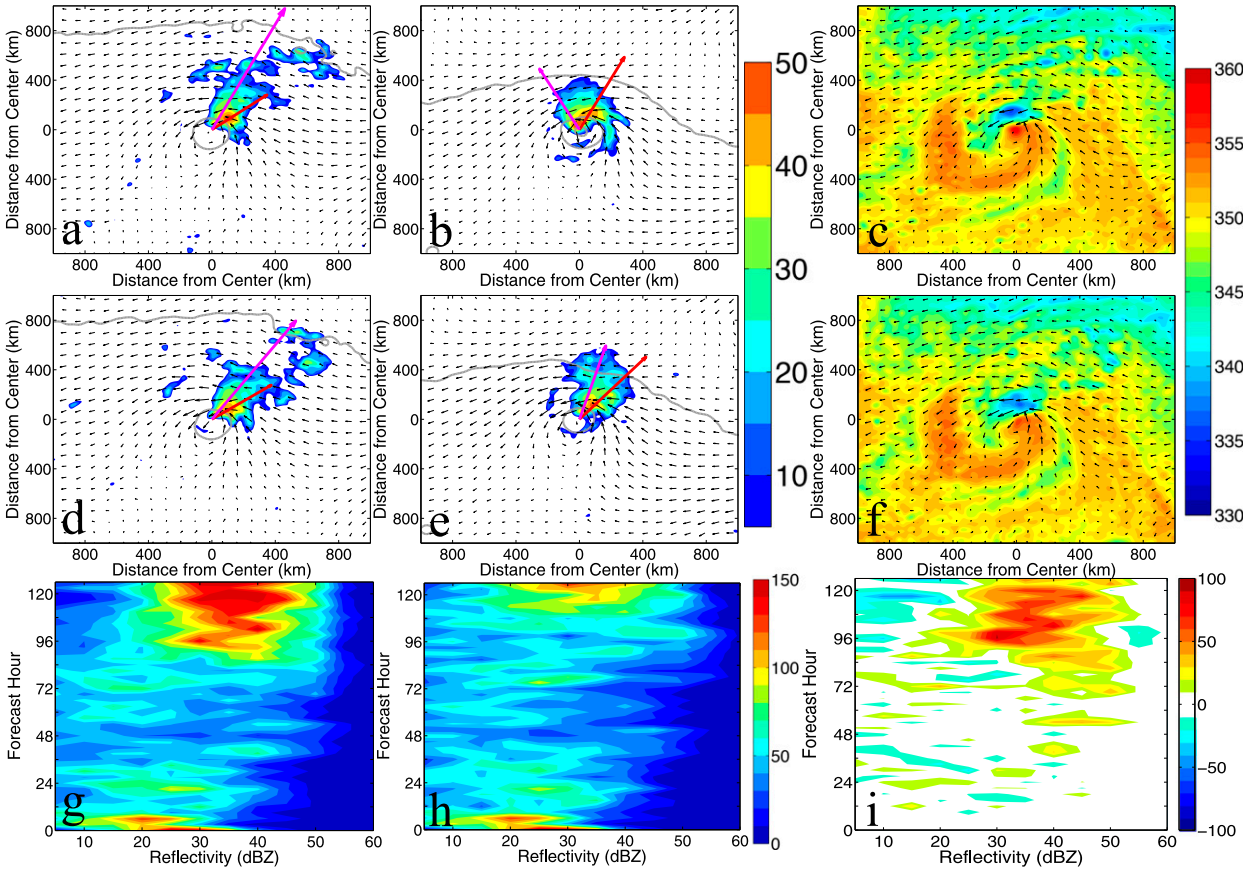

FIG. 15. Surface maps as in Fig. 8 for EnvGoodTcPoor800 at (a) 51 and (b) 84 h. (c) The 985-hPa θ_e fields (filled contours every 1 K) and surface winds (vectors) for EnvGoodTcPoor800 at 51 h. (d)–(f) As in (a)–(c), respectively, but for EnvGoodTcPoor800DiffQ. Maximum reflectivity (dBZ) frequency diagram (raw counts) for the all-quadrant convection (within 150 km of the surface center) for the 126-h (g) MemEnvGoodTcPoor800 and (h) MemEnvGoodTcPoor800DiffQ simulations. (i) Differences in maximum reflectivity frequency (filled contours every 10 between −100 and 100) between (g) and (h).

resilient to strong shear, which is consistent with previous research.

Further examination of the evolution of the deep-layer shear vector across composite groups separated by RI-onset time reveals that weaker shear results in earlier RI onset. Furthermore, ~6–12 h prior to RI in all of the developing composites, the shear magnitude begins to decrease, demonstrating that a reduction in deep-layer shear can indicate an imminent RI event if the environment is otherwise favorable. Finally, there is remarkable consistency between the composite groups that RI begins when shear decreases to 8–9 m s^{-1}.

Among the intensifying ensemble members, ~24–48 h prior to RI onset, a reduction in the tilt magnitude in the developing composites was observed. In addition, the tilt vector and the region of strongest convection are typically aligned and initially collocated in the downshear quadrant. As RI is approached, the tilt vector and the strongest convection begin to precess in a counterclockwise direction. After the tilt vector precesses into the upshear-left quadrant, a reduction in tilt magnitude results, probably due to the advection of the upper-level circulation center over the low-level center, triggering alignment and RI. Although RI-onset time varies by as much as 48 h of simulation time among intensifying members, the precession and alignment process of the developing vortices under similar profiles of deep-layer shear demonstrates that the simulations follow comparable pathways toward RI.

Results from the composited initial-conditions experiments also supported the hypothesis that the GOOD_EARLY vortices developed more quickly because they were initially stronger. This was shown in a set of experiments where the vortex of the GOOD_EARLY composited initial conditions was replaced with the initial vortex of both the GOOD (RI similar to best track) and POOR (nonintensifying) composited vortices. The resulting simulations produced storms with

RI onsets at 72 h, or 24 h after the RI onset of the original GOOD_EARLY composited simulation. Likewise, when the GOOD_EARLY vortex was inserted into the composited initial conditions of the GOOD environment, the resulting storm achieved RI earlier. In addition, when the GOOD_EARLY vortex was placed in the POOR environment, the vortex was able to intensify as quickly as that in GOOD. Thus, for these TCs embedded in a moderate-wind-shear environment, an initially stronger vortex accelerates the precession process and allows for an earlier RI onset, regardless of the environment.

The delay in development of the initially stronger GOOD_EARLY vortex embedded in the POOR environment suggests that the POOR environment is somewhat detrimental to RI. To identify the most unfavorable region of the POOR environment, additional blended initial conditions were created utilizing the GOOD and POOR composites. The radius at which the inner-core and environmental regions were combined was steadily increased from 500 to 900 km for both the GOOD inner core embedded in the POOR environment and vice versa. These experiments revealed that the region most detrimental to RI in the POOR environment was between 800 and 900 km from the surface center of Edouard.

To examine this region in the POOR environment in greater detail, an additional experiment was performed in which only the moisture field was perturbed in the sensitive region of the EnvGoodTcPoor800 initial conditions. However, this sensitivity may not be specific to moisture, and divergent behavior may occur for perturbations to other fields, such as temperature, zonal wind, or meridional wind. These small adjustments to the moisture field yielded an experiment that failed to undergo RI, while the original experiment began RI at ~72 h. A comparison of the radar reflectivity and vortex structure evolutions revealed that the two simulations were extremely similar throughout the first 48 h, with the first observable differences occurring at 51 h. In the EnvGoodTcPoor800 experiment, a stronger burst of convection near the surface center of Edouard appears to have contributed to the strengthening of the vortex-scale circulation, allowing for the tilt vector to precess counterclockwise farther toward the upshear quadrant. This difference in convective strength allows for the completion of precession and alignment of this experiment within the 5-day simulation window. Attempts to diagnose the sources of the difference in moist convective strength between the experiments proved to be difficult, which highlights the intrinsic predictability that is present in these RI scenarios.

The analysis of this ensemble simulation of Edouard has demonstrated that, despite some advances in the forecasting of RI, the predictability of RI remains limited, particularly in the moderate deep-layer shear regime. At least part of the variability in RI-onset timing results from small differences in the wind shear magnitude, which impact the magnitude of the tilt vector and the speed of the subsequent precession process. The ensemble sensitivity and composite analyses suggest that RI will not commence until the vortex has completed precession and the vortex aligns; any information that forecasters can obtain in real time about the orientation of the vortex tilt in relation to the shear may aid in the prediction of the exact timing of RI onset.

Acknowledgments. This work is supported by the NASA New Investigator Program (Grant NNX12AJ79G), the Office of Naval Research (Grant N000140910526), the National Science Foundation (Grant AGS-1305798), and NASA's Hurricane Science Research Program (HSRP) and the Hurricane and Severe Storm Sentinel (HS3) investigation under NASA's Earth Venture Program. Computing was performed at the Texas Advanced Computing Center (TACC).

REFERENCES

Barker, D. M., W. Huang, Y.-R. Guo, A. J. Bourgeois, and Q. N. Xiao, 2004: A three-dimensional variational data assimilation system for MM5: Implementation and initial results. *Mon. Wea. Rev.*, **132**, 897–914, doi:10.1175/1520-0493(2004)132<0897:ATVDAS>2.0.CO;2.

Black, M. L., J. F. Gamache, F. D. Marks, C. E. Samsury, and H. E. Willoughby, 2002: Eastern Pacific Hurricanes Jimena of 1991 and Olivia of 1994: The effect of vertical shear on structure and intensity. *Mon. Wea. Rev.*, **130**, 2291–2312, doi:10.1175/1520-0493(2002)130<2291:EPHJOA>2.0.CO;2.

Braun, S. A., and L. Wu, 2007: A numerical study of Hurricane Erin (2001). Part II: Shear and the organization of eyewall vertical motion. *Mon. Wea. Rev.*, **135**, 1179–1194, doi:10.1175/MWR3336.1.

——, M. T. Montgomery, and Z. Pu, 2006: High-resolution simulation of Hurricane Bonnie (1998). Part I: The organization of vertical motion. *J. Atmos. Sci.*, **63**, 19–42, doi:10.1175/JAS3598.1.

——, P. A. Newman, and G. M. Heymsfield, 2016: NASA's Hurricane and Severe Storm Sentinel (HS3) investigation. *Bull. Amer. Meteor. Soc.*, **97**, 2085–2102, doi:10.1175/BAMS-D-15-00186.1.

Brown, B. R., and G. J. Hakim, 2015: Sensitivity of intensifying Atlantic hurricanes to vortex structure. *Quart. J. Roy. Meteor. Soc.*, **141**, 2538–2551, doi:10.1002/qj.2540.

Chen, H., and S. G. Gopalakrishnan, 2015: A study on the asymmetric rapid intensification of Hurricane Earl (2010) using the HWRF system. *J. Atmos. Sci.*, **72**, 531–550, doi:10.1175/JAS-D-14-0097.1.

Chen, S. S., J. A. Knaff, and F. D. Marks Jr., 2006: Effects of vertical wind shear and storm motion on tropical cyclone rainfall

asymmetries deduced from TRMM. *Mon. Wea. Rev.*, **134**, 3190–3208, doi:10.1175/MWR3245.1.

Corbosiero, K. L., and J. Molinari, 2002: The effects of vertical wind shear on the distribution of convection in tropical cyclones. *Mon. Wea. Rev.*, **130**, 2110–2123, doi:10.1175/1520-0493(2002)130<2110:TEOVWS>2.0.CO;2.

——, and ——, 2003: The relationship between storm motion, vertical wind shear, and convective asymmetries in tropical cyclones. *J. Atmos. Sci.*, **60**, 366–376, doi:10.1175/1520-0469(2003)060<0366:TRBSMV>2.0.CO;2.

DeMaria, M., M. Mainelli, L. K. Shay, J. A. Knaff, and J. Kaplan, 2005: Further improvements to the Statistical Hurricane Intensity Prediction System (SHIPS). *Wea. Forecasting*, **20**, 531–543, doi:10.1175/WAF862.1.

Elsberry, R. L., T. D. B. Lambert, and M. A. Boothe, 2007: Accuracy of Atlantic and eastern North Pacific tropical cyclone intensity forecast guidance. *Wea. Forecasting*, **22**, 747–762, doi:10.1175/WAF1015.1.

Frank, W. M., and E. A. Ritchie, 1999: Effects of environmental flow upon tropical cyclone structure. *Mon. Wea. Rev.*, **127**, 2044–2061, doi:10.1175/1520-0493(1999)127<2044:EOEFUT>2.0.CO;2.

——, and ——, 2001: Effects of vertical wind shear on the intensity and structure of numerically simulated hurricanes. *Mon. Wea. Rev.*, **129**, 2249–2269, doi:10.1175/1520-0493(2001)129<2249:EOVWSO>2.0.CO;2.

Green, B. W., and F. Zhang, 2013: Impacts of air–sea flux parameterizations on the intensity and structure of tropical cyclones. *Mon. Wea. Rev.*, **141**, 2308–2324, doi:10.1175/MWR-D-12-00274.1.

Jones, S. C., 1995: The evolution of vortices in vertical shear. I: Initially barotropic vortices. *Quart. J. Roy. Meteor. Soc.*, **121**, 821–851, doi:10.1002/qj.49712152406.

Kaplan, J., and M. DeMaria, 2003: Large-scale characteristics of rapidly intensifying tropical cyclones in the North Atlantic basin. *Wea. Forecasting*, **18**, 1093–1108, doi:10.1175/1520-0434(2003)018<1093:LCORIT>2.0.CO;2.

——, ——, and J. A. Knaff, 2010: A revised tropical cyclone rapid intensification index for the Atlantic and eastern North Pacific basins. *Wea. Forecasting*, **25**, 220–241, doi:10.1175/2009WAF2222280.1.

Komaromi, W. A., S. J. Majumdar, and E. D. Rappin, 2011: Diagnosing initial condition sensitivity of Typhoon Sinlaku (2008) and Hurricane Ike (2008). *Mon. Wea. Rev.*, **139**, 3224–3242, doi:10.1175/MWR-D-10-05018.1.

Munsell, E. B., and F. Zhang, 2014: Prediction and uncertainty of Hurricane Sandy (2012) explored through a real-time cloud-permitting ensemble analysis and forecast system assimilating airborne Doppler radar observations. *J. Adv. Model. Earth Syst.*, **6**, 38–58, doi:10.1002/2013MS000297.

——, ——, and D. P. Stern, 2013: Predictability and dynamics of a nonintensifying tropical storm: Erika (2009). *J. Atmos. Sci.*, **70**, 2505–2524, doi:10.1175/JAS-D-12-0243.1.

——, J. A. Sippel, S. A. Braun, Y. Weng, and F. Zhang, 2015: Dynamics and predictability of Hurricane Nadine (2012) evaluated through convection-permitting ensemble analysis and forecasts. *Mon. Wea. Rev.*, **143**, 4514–4532, doi:10.1175/MWR-D-14-00358.1.

Rappin, E. D., and D. S. Nolan, 2012: The effect of vertical shear orientation on tropical cyclogenesis. *Quart. J. Roy. Meteor. Soc.*, **138**, 1035–1054, doi:10.1002/qj.977.

Reasor, P. D., and M. T. Montgomery, 2001: Three-dimensional alignment and corotation of weak, TC-like vortices via linear vortex Rossby waves. *J. Atmos. Sci.*, **58**, 2306–2330, doi:10.1175/1520-0469(2001)058<2306:TDAACO>2.0.CO;2.

——, ——, and L. D. Grasso, 2004: A new look at the problem of tropical cyclones in vertical shear flow: Vortex resiliency. *J. Atmos. Sci.*, **61**, 3–22, doi:10.1175/1520-0469(2004)061<0003:ANLATP>2.0.CO;2.

Rogers, R. F., S. Chen, J. Tenerelli, and H. Willoughby, 2003: A numerical study of the impact of vertical shear on the distribution of rainfall in Hurricane Bonnie (1998). *Mon. Wea. Rev.*, **131**, 1577–1598, doi:10.1175//2546.1.

——, P. D. Reasor, and J. A. Zhang, 2015: Multiscale structure and evolution of Hurricane Earl (2010) during rapid intensification. *Mon. Wea. Rev.*, **143**, 536–562, doi:10.1175/MWR-D-14-00175.1.

——, J. A. Zhang, J. Zawislak, H. Jiang, G. R. Alvey III, E. J. Zipser, and S. N. Stevenson, 2016: Observations of the structure and evolution of Hurricane Edouard (2014) during intensity change. Part II: Kinematic structure and the distribution of deep convection. *Mon. Wea. Rev.*, **144**, 3355–3376, doi:10.1175/MWR-D-16-0017.1.

Sippel, J. A., S. A. Braun, and C.-L. Shie, 2011: Environmental influences on the strength of Tropical Storm Debby (2006). *J. Atmos. Sci.*, **68**, 2557–2581, doi:10.1175/2011JAS3648.1.

Skamarock, W. C., and Coauthors, 2008: A description of the Advanced Research WRF version 3. NCAR Tech. Note NCAR/TN–4751STR, 113 pp., doi:10.5065/D68S4MVH.

Stewart, S. R., 2014: Tropical cyclone report: Hurricane Edouard (AL062014). NOAA/National Hurricane Center Tech. Rep. AL062014, 19 pp. [Available online at http://www.nhc.noaa.gov/data/tcr/AL062014_Edouard.pdf.]

Tang, X., and F. Zhang, 2016: Impacts of the diurnal radiation cycle on the formation, intensity and structure of Hurricane Edouard (2014). *J. Atmos. Sci.*, **73**, 2871–2892, doi:10.1175/JAS-D-15-0283.1.

Tao, D., and F. Zhang, 2014: Effect of environmental shear, sea-surface temperature and ambient moisture on the formation and predictability of tropical cyclones: An ensemble-mean perspective. *J. Adv. Model. Earth Syst.*, **6**, 384–404, doi:10.1002/2014MS000314.

——, and ——, 2015: Effects of vertical wind shear on the predictability of tropical cyclones: Practical versus intrinsic limit. *J. Adv. Model. Earth Syst.*, **7**, 1534–1553, doi:10.1002/2015MS000474.

Torn, R. D., and G. J. Hakim, 2009: Initial condition sensitivity of western Pacific extratropical transitions determined using ensemble-based sensitivity analysis. *Mon. Wea. Rev.*, **137**, 3388–3406, doi:10.1175/2009MWR2879.1.

——, and D. Cook, 2013: The role of vortex and environment errors in genesis forecasts of Hurricanes Danielle and Karl (2010). *Mon. Wea. Rev.*, **141**, 232–251, doi:10.1175/MWR-D-12-00086.1.

——, J. S. Whitaker, P. Pegion, T. M. Hamill, and G. J. Hakim, 2015: Diagnosis of the source of GFS medium-range track errors in Hurricane Sandy (2012). *Mon. Wea. Rev.*, **143**, 132–152, doi:10.1175/MWR-D-14-00086.1.

Velden, C. S., and L. M. Leslie, 1991: The basic relationship between tropical cyclone intensity and the depth of the environmental steering layer in the Australian region. *Wea. Forecasting*, **6**, 244–253, doi:10.1175/1520-0434(1991)006<0244:TBRBTC>2.0.CO;2.

Weng, Y., and F. Zhang, 2012: Assimilating airborne Doppler radar observations with an ensemble Kalman filter for convection-permitting hurricane initialization and prediction: Katrina (2005). *Mon. Wea. Rev.*, **140**, 841–859, doi:10.1175/2011MWR3602.1.

——, and ——, 2016: Advances in convection-permitting tropical cyclone analysis and prediction through EnKF assimilation of reconnaissance aircraft observations. *J. Meteor. Soc. Japan*, **4**, 345–358, doi:10.2151/jmsj.2016-018.

Wick, G., 2015: Hurricane and Severe Storm Sentinel (HS3) Global Hawk AVAPS dropsonde system, version 2014 RF05–08. NASA Global Hydrology Resource Center Distributed Active Archive Center, accessed 16 September 2016, doi:10.5067/HS3/AVAPS/DROPSONDE/DATA201.

Young, K., T. Hock, and C. Martin, 2016: Hurricane and Severe Storm Sentinel (HS3) 2014 dropsonde data quality report. Version 3.0, National Center for Atmospheric Research (NCAR) Earth Observing Lab (EOL), accessed 16 September 2016. [Available online at http://data.eol.ucar.edu/datafile/nph-get/348.004/readme.V3.HS3-2014.GHdropsonde.pdf.]

Zhang, F., and J. A. Sippel, 2009: Effects of moist convection on hurricane predictability. *J. Atmos. Sci.*, **66**, 1944–1961, doi:10.1175/2009JAS2824.1.

——, and D. Tao, 2013: Effects of vertical wind shear on the predictability of tropical cyclones. *J. Atmos. Sci.*, **70**, 975–983, doi:10.1175/JAS-D-12-0133.1.

——, and Y. Weng, 2015: Predicting hurricane intensity and associated hazards: A five-year real-time forecast experiment with assimilation of airborne Doppler radar observations. *Bull. Amer. Meteor. Soc.*, **96**, 25–32, doi:10.1175/BAMS-D-13-00231.1.

——, ——, J. A. Sippel, Z. Meng, and C. H. Bishop, 2009: Cloud-resolving hurricane initialization and prediction through assimilation of Doppler radar observations with an ensemble Kalman filter: Humberto (2007). *Mon. Wea. Rev.*, **137**, 2105–2125, doi:10.1175/2009MWR2645.1.

——, ——, J. F. Gamache, and F. D. Marks, 2011: Performance of convection-permitting hurricane initialization and prediction during 2008–2010 with ensemble data assimilation of inner-core airborne Doppler radar observations. *Geophys. Res. Lett.*, **38**, L15810, doi:10.1029/2011GL048469.